UNIVERSITY OF CALGARY

MIL-100(Fe)-Based Composites for Photocatalytic Dye Degradation: Harnessing UV and Visible Light with Enhanced Performance

by

Seyedehfateme Hosseini

A THESIS

SUBMITTED TO THE FACULTY OF GRADUATE STUDIES

IN PARTIAL FULFILMENT OF THE REQUIREMENTS FOR THE

DEGREE OF MASTER OF SCIENCE

GRADUATE PROGRAM IN MECHANICAL ENGINEERING

CALGARY, ALBERTA

JULY, 2024

Abstract

This study explores the photocatalytic degradation efficiencies MIL-100(Fe)-Based composites under both UV and visible light. The synthesized ZnO/MIL-100(Fe), ZnO/Ni@MIL photocatalysts were assessed based on their ability to degrade Rhodamine 6G (R6G), a cationic dye. The main aim of integrating MIL-100(Fe) into ZnO nanoparticles is to enhance the surface area of the photocatalyst to improve adsorption and photocatalytic performance, which is crucial for effective dye degradation. Under UV light, ZnO/MIL-100(Fe) exhibited the highest degradation efficiency, achieving complete degradation within 60 minutes. This exceptional performance is attributed to the enhanced adsorption and charge separation and transfer between ZnO and MIL-100(Fe). ZnO/Ni@MIL-100(Fe) followed closely with a 96% degradation efficiency, highlighting the role of Ni nanoparticles in enhancing photocatalytic performance through improved adsorption kinetics and charge carrier dynamics. Under visible light, ZnO/Ni@MIL-100(Fe) demonstrated the highest efficiency, reaching nearly 98% degradation within 60 minutes following by ZnO/MIL-100(Fe) with 88% degradation efficiency. This superior performance is due to the synergistic effects of enhanced light absorption and electron scavenging of Ni nanoparticles. Both synthesized composites exhibit significantly higher efficiency compared to ZnO NPs, MIL-100(Fe), and Ni@MIL-100(Fe). The findings suggest that ZnO/Ni@MIL-100(Fe) is a highly effective photocatalyst under visible light, while ZnO/MIL-100(Fe) excels under UV light. This study underscores the potential of these composites for practical applications in environmental remediation, driven by their enhanced photocatalytic activities and adsorption properties, primarily due to the increased surface area provided by MOFs.

Acknowledgements

I am profoundly grateful to my supervisor, Dr. Seonghwan Kim, for his invaluable guidance, support, and encouragement throughout my research journey. Dr. Kim placed his trust in me from the very outset, offering me an opportunity when I was a newly graduated undergraduate with limited experience. His faith in my potential and his dedication to my academic and professional development have been immensely inspiring. Dr. Kim's expertise and insights have been pivotal in shaping this thesis.

I am also immensely thankful to my examiners, Dr. Nader Mahinpey and Dr. Keekyoung Kim. They made time to be my examiners and generously shared their knowledge to help me improve my work. Their patience and support have been greatly appreciated. Special thanks to Dr. Brian Baillie the technician and Shokoufeh Manouchehr the lab manager in CERC team at the University of Calgary for their support and assistance with running the ICP and BET analysis, which were crucial for my research. I acknowledge the support of the Natural Sciences and Engineering Research Council of Canada (NSERC) Discovery Grant (RGPIN-03943-2020) and the Canada Research Chairs Program (CRC-2020-00322). I would also like to acknowledge my labmates, Pegah Zandi and Setareh Homayoonnia, for their guidance and help in the lab. Their constant support and willingness to share knowledge made the research process smoother and more enjoyable. Additionally, I am thankful to my friends, Nima Tabatabaei and Ehsan Moharreri for his support and advice, which have been invaluable throughout my studies.

A heartfelt thank you to my supportive fiancé, Moein, who stood by me during the challenging times and provided support. His encouragement and understanding have been a constant source of strength. Lastly, I am forever indebted to my family, who, despite being far away, always believed in me and encouraged me to pursue my dreams. Their love and faith in my abilities have been my greatest motivators.

Dedication

This thesis is dedicated to my fiancé Moein, For his support and belief in me through every challenge and success. This work is dedicated to you, for always being there, for lifting me up when I faltered, and for believing in me even when I doubted myself. Thank you for being my rock and my inspiration.

Table of Contents

List of Tables

List of Illustrations, Figures, & Graphics

List of Symbols, Abbreviations, & Nomenclature

Symbol	Description	Units
MIL-100(Fe)	Metal-Organic Framework with Iron	-
ZnO	Zinc Oxide	-
Ni@MIL-100(Fe)	Nickel nanoparticles encapsulated in MIL-100(Fe)	-
ZnO/MIL-100(Fe)	Composite of Zinc Oxide and MIL-100(Fe)	-
ZnO/Ni@MIL-100(Fe)	Composite of Zinc Oxide and Nickel nanoparticles in MIL-100(Fe)	-
R6G	Rhodamine 6G Dye	-
UV	Ultraviolet Light	-
ICP-MS	Inductively Coupled Plasma Mass Spectrometry	-
XRD	X-Ray Diffraction	-
TGA	Thermogravimetric Analysis	-
SEM	Scanning Electron Microscopy	-
TEM	Transmission Electron Microscopy	-
UV-vis	Ultraviolet-visible Spectroscopy	-
BET	Brunauer-Emmett-Teller Surface Area Analysis	-
ROS	Reactive Oxygen Species	-
$O_2^{\bullet -}$	Superoxide Anion	-

•OH	Hydroxyl Radical	-
η	Degradation Efficiency	%
k	Rate Constant	min^{-1}
S_{BET}	BET Surface Area	m^2/g
V_p	Pore Volume	cm^3/g
D	Average Pore Diameter	nm
q_t	Quantity Adsorbed per Unit Mass	mg/g
C_o	Initial Concentration of R6G Dye	mg/L
C_e	Equilibrium Concentration of R6G Dye	mg/L
V	Volume of Solution	L
m	Mass of Adsorbent	g
hν	Photon Energy	eV
E_g	Band Gap Energy	eV
α	Absorption Coefficient	cm^{-1}
h	Planck's Constant	J·s
ν	Frequency of Light	Hz
B	Proportionality Constant	-
e_{CB}^-	Conduction Band Electron	-
h_{VB}^+	Valence Band Hole	-

Statement of Contribution

Seyedehfateme Hosseini was responsible for conducting all aspects of the research, including the literature review, experimental design, data collection, data analysis, and the writing of the manuscript. Professor. Seonghwan Kim made significant contributions to the generation of ideas, the design of experiments, and the analysis of data. Moreover, he offered invaluable guidance and feedback throughout the research process and played a key role in revising the manuscript.

Chapter 1: Introduction

1.1 Problem Statement

In recent decades, water pollution resulting from rapid industrialization and human activities has posed significant threats to both human health and the environment. The main culprit behind water pollution is textile industry by releasing intricate blends of colored and potentially harmful substances into water ways. These pollutants often find their way into rivers and streams, lowering water quality. Statistics from the World Bank demonstrates that textile dyeing, and treatment processes contribute to about 17-20% of industrial water pollution. Given that only 47% of synthetic dyes are biodegradable, their presence in aquatic environments poses a critical threat to aquatic life [1, 2]. Not only do they interfere with natural light processes, but they also present major risks to aquatic life by introducing toxic compounds into the water bodies. Efforts to mitigate the impact of dye discharge have faced considerable challenges. Despite improvements in dyeing techniques aimed at minimizing residual dye content, the issue of colored wastewater persists [3]. Conventional water treatment methods struggle to effectively tackle the chemical complexity and stability of synthetic organic dyes, which resist degradation and are stable in water [4]. Initially, various conventional chemical methods such as coagulation-flocculation and precipitation were employed to address the issue. However, their low efficiency (less than 30%), generation of harmful by-products, and the substantial time and financial investments required have hindered their applicability [5]. This highlights the need for innovative strategies to effectively manage their widespread production and address their toxicity. In this regard, photocatalytic degradation has appeared as a promising solution in recent years for its ability to completely eliminate organic dyes from wastewater, cost-effectiveness, minimal secondary pollution and without necessitating the application of chemical substances, intensive energy, and time investments [6]. This has led to photocatalysis being regarded as an economical and environmentally friendly alternative to traditional methods [7].

1.2 Significance

This study employs MIL-100(Fe)-based composites, specifically ZnO/MIL-100(Fe) and ZnO/Ni@MIL-100(Fe), as effective photocatalysts for the degradation of Rhodamine 6G (R6G). The novelty of this work is attributed to the integration of ZnO and Ni nanoparticles onto the MIL-100(Fe) framework for the first time to investigate its advancement in photocatalytic degradation research due to the unique properties and superior performance of these composites. Incorporating ZnO into the MIL-100(Fe) structure provides synergistic effects, leading to improved charge separation, reduced recombination rates, and increased surface area for enhanced dye degradation. The addition of Ni nanoparticles further enhances these properties by improving light absorption, adsorption kinetics and facilitating charge carrier dynamics. The main aim of this project focuses on addressing the limitations of zinc oxide nanoparticles (ZnO NPs) as a common photocatalyst for dye degradation, such as low surface area and rapid electron-hole recombination. The composite formed by incorporating ZnO into MIL-100(Fe) offers an improved adsorption surface due to the presence of pores, thereby providing a more active surface for the photocatalytic reaction. Unlike common photocatalysts, these composites do not require the addition of substances like H_2O_2 to achieve high efficiency, and the photocatalyst concentration/R6G concentration ratio is reasonable, further emphasizing their practicality and cost-effectiveness. Furthermore, the degradation process is rapid, with ZnO/MIL-100(Fe) achieving complete degradation within 60 minutes under UV light, and ZnO/Ni@MIL-100(Fe) demonstrating nearly 98% degradation under visible light. This improved efficiency is highlighted by the composites' ability to achieve high degradation percentages in significantly shorter times compared to other works. This research contributes to advancing photocatalytic degradation technologies and offers insights into the development of highly efficient and environmentally friendly photocatalysts for water pollution remediation. The findings suggest ZnO/MIL-100(Fe) and ZnO/Ni@MIL-100(Fe) composites as potential photocatalysts for environmental cleanup, driven by their enhanced photocatalytic activities, adsorption properties, and practical usability.

1.3 Research Questions

- How does the incorporation of ZnO and Ni nanoparticles into the MIL-100(Fe) framework enhance the photocatalytic degradation efficiency of Rhodamine 6G?

- What role do Ni nanoparticles play in improving the adsorption kinetics and charge carrier dynamics in the ZnO/Ni@MIL-100(Fe) composite for visible light photocatalysis?

- How do the structural and morphological characteristics of MIL-100(Fe) contribute to its overall photocatalytic performance when combined with ZnO and Ni nanoparticles?

- What are the comparative degradation efficiencies of Rhodamine 6G using ZnO/MIL-100(Fe) and ZnO/Ni@MIL-100(Fe) composites under both UV and visible light conditions?

- How does the surface area and pore structure of MIL-100(Fe) influence the adsorption capacity and photocatalytic activity of the synthesized composites?

- What are the mechanisms behind the enhanced photocatalytic degradation of Rhodamine 6G in the presence of ZnO/Ni@MIL-100(Fe) compared to ZnO/MIL-100(Fe)?

- How does varying the concentration of ZnO and Ni nanoparticles in the MIL-100(Fe) framework affect the overall photocatalytic efficiency and stability of the composites?

- How do changes in pH, dye concentration, and catalyst concentration influence the photocatalytic degradation efficiency of Rhodamine 6G using ZnO/MIL-100(Fe) and ZnO/Ni@MIL-100(Fe) composites?

- What are the recovery and reusability characteristics of ZnO/MIL-100(Fe) and ZnO/Ni@MIL-100(Fe) photocatalysts over multiple degradation cycles of Rhodamine 6G?

1.4 Research Aims

The principal objective of this research is to investigate the potential of ZnO/MIL-100(Fe) and ZnO/Ni@MIL-100(Fe) composites as cost-effective and highly efficient photocatalysts for the degradation of Rhodamine 6G. Emphasizing their remarkable efficiency, stability, and practicality under both UV and visible light, this study aims to provide an environmentally sustainable solution to address dye pollution in water systems by utilizing advanced composite materials.

1.5 Specific Objectives

To achieve the stated goal, the following objectives were pursued:

- Objective 1: To synthesize and characterize various photocatalysts, including ZnO nanoparticles (ZnO NPs), MIL-100(Fe), ZnO/MIL-100(Fe), and ZnO/Ni@MIL-100(Fe).

- Objective 2: To investigate the influence of different amounts of ZnO nanoparticles loaded into the MIL-100(Fe) framework on the degradation efficiency of Rhodamine 6G.

- Objective 3: To evaluate the effect of varying amounts of photocatalyst on the degradation efficiency of Rhodamine 6G.

- Objective 4: To assess the impact of different initial pH levels of the reaction solution on the degradation efficiency of Rhodamine 6G.

- Objective 5: To explore the effect of different light sources (UV and visible light) on the photocatalytic degradation of Rhodamine 6G.

- Objective 6: To conduct calibration tests for Rhodamine 6G concentration to ensure accurate measurement of degradation efficiency.

- Objective 7: To evaluate the overall efficiency, stability, and reusability of the synthesized photocatalysts in the degradation of Rhodamine 6G.

- Objective 8: To understand the degradation pathways and mechanisms involved in the photocatalytic process, focusing on the roles of reactive oxygen species (ROS) generated during the reaction.

By achieving these objectives, this research aims to advance the field of photocatalytic degradation technologies and provide insights into the development of highly efficient and environmentally friendly photocatalysts for water pollution remediation.

Chapter 2: MIL-100(Fe)-Based Photocatalysts for Rhodamine 6G Degradation: Harnessing UV and Visible Light with Enhanced Performance

Seyedehfateme Hosseini, Seonghwan Kim *

Department of Mechanical and Manufacturing Engineering, University of Calgary, Calgary, Alberta T2N 1N4, Canada

*E-mail: sskim@ucalgary.ca

Abstract: This study explores the photocatalytic degradation efficiencies MIL-100(Fe)-Based composites under both UV and visible light. The synthesized ZnO/MIL-100(Fe), ZnO/Ni@MIL photocatalysts were assessed based on their ability to degrade Rhodamine 6G (R6G) as a pollution model. The main aim of integrating MIL-100(Fe) into ZnO nanoparticles is to enhance the surface area of the ZnO NPs to improve adsorption and enhancing electron-hole separation to improve photocatalytic performance, which is crucial for effective dye degradation. Under UV light, ZnO/MIL-100(Fe) exhibited the highest degradation efficiency, achieving complete degradation within 60 minutes. ZnO/Ni@MIL-100(Fe) followed closely with a 96% degradation efficiency. Under visible light, ZnO/Ni@MIL-100(Fe) demonstrated the highest efficiency, reaching nearly 98% degradation within 60 minutes. This exceptional performance is attributed to the synergistic effects arising from enhanced light absorption, improved adsorption kinetics, optimized charge carrier dynamics, and effective electron scavenging, all of which result from the addition of ZnO and Ni nanoparticles to the composite. Both synthesized composites exhibit significantly higher efficiency compared to ZnO NPs, MIL-100(Fe), and Ni@MIL-100(Fe). The findings suggest that ZnO/Ni@MIL-100(Fe) is a highly effective photocatalyst under visible light, while ZnO/MIL-100(Fe) excels under UV light. This study underscores the potential of these composites for practical applications in environmental remediation, driven by their enhanced photocatalytic activities and adsorption properties, primarily due to the increased surface area provided by MOFs.

Keywords: metal-organic frameworks (MOFs); Adsorption; photocatalytic degradation; Rhodamine 6G dye

2.1 Introduction

In recent decades, water pollution resulting from rapid industrialization and human activities has posed significant threats to both human health and the environment. The main culprit behind water pollution is textile industry by releasing intricate blends of colored and potentially harmful substances into water ways. These pollutants often find their way into rivers and streams, lowering water quality. Statistics from the World Bank demonstrates that textile dyeing, and treatment processes contribute to about 17-20% of industrial water pollution. Given that only 47% of synthetic dyes are biodegradable, their presence in aquatic environments poses a critical threat to aquatic life [1, 2]. Not only do they interfere with natural light processes, but they also present major risks to aquatic life by introducing toxic compounds into the water bodies. Efforts to mitigate the impact of dye discharge have faced considerable challenges. Despite improvements in dyeing techniques aimed at minimizing residual dye content, the issue of colored wastewater persists [3]. Conventional water treatment methods struggle to effectively tackle the chemical complexity and stability of synthetic organic dyes, which resist degradation and are stable in water [4]. Initially, various conventional chemical methods such as coagulation-flocculation and precipitation were employed to address the issue. However, their low efficiency (less than 30%), generation of harmful by-products, and the substantial time and financial investments required have hindered their applicability [5, 6]. This highlights the need for innovative strategies to effectively manage their widespread production and address their toxicity. In this regard, photocatalytic degradation has appeared as a promising solution in recent years for its ability to eliminate organic dyes from wastewater, cost-effectiveness, minimal secondary pollution and without necessitating the application of chemical substances, intensive energy, and time investments [7]. This has led to photocatalysis being regarded as an economical and environmentally friendly alternative to traditional methods [8]. The photodegradation process involves the adsorption of dye molecules onto the photocatalyst surface and their breakdown by reactive radicals. In this method, after absorbing photons by the photocatalyst, a chain reaction unfolds. The electrons within the material absorb the energy from the photons, becoming excited and transitioning from the valence band to the conduction band, thus generating electron-hole pairs. These pairs, consisting of excited electrons and the positively charged holes they leave behind, have the ability to travel towards the surface of the photocatalyst [9]. There, they participate in a sequence of redox reactions, with electrons driving

reduction processes and holes catalyzing oxidation reactions. This coordinated interplay of charge carriers leads to the creation of highly reactive substances, including superoxide anions (•O2-) formed through interactions between electrons and oxygen, and hydroxyl radicals (•OH) formed through interactions between holes and water molecules [3]. These radicals play a critical role in breaking down a diverse array of environmental pollutants, ranging from contaminants and organic compounds to bacteria and viruses [10]. The photocatalytic reactions can be influenced by several operational variables such as the initial concentration of the dye, catalyst concentration and the pH of the solution [11, 12]. For instance, zinc oxide (ZnO) was employed as the photocatalyst in a study investigating the impact of various operational variables on the photocatalytic degradation of Rhodamine B dye. The study found that higher initial dye concentrations reduced degradation efficiency, while longer contact times and optimal material doses improved it [11]. In another study It was found that higher initial dye concentrations can increase adsorption but may saturate active sites, reducing efficiency. Optimal pH conditions enhance interactions between dye and photocatalyst, while reaction temperature affects molecular kinetic energy and catalyst stability. Additionally, light intensity plays a crucial role, with higher intensities boosting energy for the process but potentially causing photodamage or reducing catalyst lifetime [12]. One of the common photocatalysts is TiO_2 due to its suitable band gap energies, chemical stability, strong redox potentials [13]. However, TiO_2 possesses a relatively large band gap energy, restricting its ability to absorb solar radiation to the UV light range, which constitutes only about 5% of the solar spectrum [14]. Additionally, TiO_2 suffers from significant electron-hole recombination and requires costly modifications to improve its efficiency [15]. In contrast, ZnO NPs has a slightly narrower band gap, enabling it to absorb a broader range of UV and some visible light, thereby utilizing a larger portion of solar radiation. ZnO also exhibits superior charge carrier mobility, facilitating efficient charge separation and reducing recombination rates. Furthermore, its abundance and cost-effectiveness enhance its appeal for large-scale applications [16]. However, ZnO also has limitations such as limited surface area and photo corrosion, which can reduce its stability and efficiency under illumination [17, 18]. To address these issues and enhance photocatalytic performance, researchers make composites with metal-organic frameworks (MOFs). MOFs are porous materials composed of metal ions or clusters coordinated to organic ligands, forming a highly ordered, crystalline structure with an exceptionally high surface area and tunable porosity [19]. MOFs provide a high

surface area and porosity, improving the adsorption of the target molecules facilitating greater interaction with pollutants and improving dispersion of ZnO nanoparticles [20]. Additionally, the composite structure helps enhance electron-hole recombination, leading to improved overall efficiency and stability of ZnO photocatalysts [21]. In recent years, researchers have increasingly explored metal-organic framework (MOF) based composites for their potential as efficient adsorbents and photocatalysts. One notable example is the study on the HF-free synthesis of nanoscale metal-organic framework NMIL-100(Fe) by Shengxia Duan et al. This research highlights the development of NMIL-100(Fe) using a hydrofluoric acid (HF)-free solvothermal method, resulting in a material with comparable physicochemical properties as an efficient dye adsorbent [20]. Additionally, Rajnish Kaur et al. investigated a novel hybrid structure of Eu-MOF and CdTe quantum dots (QDs) as photocatalysts. Their study focused on the synthesis and characterization of a QD/Eu-MOF nanocomposite, which combines the porous properties of the MOF matrix with the functional characteristics of encapsulated QDs. This QD/Eu-MOF nanocomposite demonstrated efficient photocatalytic degradation of Rhodamine 6G dye, achieving complete degradation within 50 minutes [22]. Many metal-organic frameworks (MOFs) are highly sensitive to moisture and exhibit structural instability in aqueous environments [23]. Consequently, there is a strong need for water-stable MOFs or MOF-based materials for effective wastewater treatment. Among the various MOFs, MIL-100(Fe) has gained significant attention due to its outstanding water stability, making it a promising option for a wide range of applications [24]. Studies have shown that MIL-100(Fe) can maintain its structural integrity under varying water vapor pressures and even withstand boiling water treatments [25]. MIL-100(Fe) is a crystalline three-dimensional material synthesized from a combination of iron (III) salt and the tricarboxylate ligand (trimesic acid) [26]. This structure causes to efficient ligand-to-metal charge-transfer transitions which makes MIL-100(Fe) an efficient photocatalyst [27]. Katrien G. M. Laurier et al. conducted a study on iron (III)-based metal-organic frameworks (MOFs) as visible light photocatalysts. While iron (III) oxides are promising due to their small band gap, their high electron-hole recombination rate limits their efficiency. Laurier and colleagues addressed this by exploring MOFs containing Fe3-μ3-oxo clusters. They demonstrated the remarkable photocatalytic efficiency of these Fe (III)-based MOFs in degrading Rhodamine 6G under visible light (350-850 nm) [19]. Another way to tackle this problem is to add metallic nanoparticles to these composites to enhance their performance.

Metallic nanoparticles act as electron sink, prolonging the electron-hole recombination time and thereby improving the overall photocatalytic efficiency. This approach not only addresses the recombination issue but also leverages the synergistic effects of metal nanoparticles, metal oxides, and MOFs to develop more effective photocatalysts [28]. Noble metals like platinum (Pt), rhodium (Rh), and palladium (Pd) are commonly used as co-catalysts in photoreactions due to their high efficiency in extracting photoinduced charges to the surface. However, the high cost and scarcity of these metals drive the search for low-cost, efficient alternatives, including non-noble metals, graphene, and sulfides. Recently, nickel has gained significant attention as a promising, affordable metal co-catalyst for photocatalytic reactions [29]. Krishnapriya et al. investigated the fabrication of dye-sensitized solar cells using various nanostructured TiO_2 incorporated with Ni nanocomposites. The synthesized nanocomposites effectively trapped incident light and enhanced electron-hole pair formation [30]. In this work, we employed ZnO as a semiconductor and formed a composite with MIL-100(Fe), subsequently enhancing the adsorption and degradation efficiency of the composite by incorporating Ni nanoparticles (Ni NPs).

2.2 Materials and methods

2.2.1 Materials

The salts of nickel(II) chloride hexahydrate (NiCl2·6H2O, ≥98%), and iron(III) chloride hexahydrate (FeCl3·6H2O, 98.0-102.0%), as well as trimesic acid (BTC, 95%), thioglycolic acid (for synthesis), ethylene glycol (≥99%), mercaptoacetic acid (MAA), Sodium hydroxide (NaOH), sulfuric acid (H_2SO_4), Sodium borohydride ($NaBH_4$), zinc oxide (ZnO, nanopowder, <100 nm particle size), and Rhodamine 6G (R6G) dye, were obtained from Sigma-Aldrich, Canada. Distilled water was used throughout the entire experiment for washing and preparing solutions. Additional chemicals for scavenger tests, including silver nitrate (AgNO3), were obtained from Sigma-Aldrich. Isopropyl alcohol (IPA) was obtained from VWR, and p-benzoquinone (BQ) was obtained from Thermo Scientific Chemicals. All chemicals were used as received without further purification.

2.2.2 Synthesis

2.2.2.1 Ni NPs Synthesis

Nickel nanoparticles (Ni NPs) were synthesized using the following procedure. First, 0.25 g of $NiCl_2 \cdot 6H_2O$ was dissolved in 30 mL of deionized water (DW). At this temperature, 20 mL of hydrazine monohydrate (N_2H_4) was added and maintained for 2 minutes to homogenize the solution and form Ni-hydrazine complexes. Subsequently, 0.838 g of NaOH dissolved in 10 mL of deionized water was added to the Ni precursor solution to adjust the pH to 12, as Ni complexes are reduced more effectively at this pH (Reaction 1) Then, 3 mL of ethylene glycol and 0.002 g of $NaBH_4$ were added to the mixture. Ethylene glycol served as both a reducing agent and a stabilizing agent to prevent agglomeration, while $NaBH_4$ acted as a nucleating and reducing agent, facilitating the formation of Ni nanoparticles [31, 32]. The mixture was then continuously stirred using a magnetic stirrer while being heated at 65°C. The resulting black powder was collected by centrifugation, washed several times with deionized water, and dried under vacuum at 60°C.

$$2Ni^{2+} + N_2H_4 + 4OH^- \rightarrow 2Ni + N_2 + 4H_2O \quad (1)$$

2.2.2.2 MIL-100(Fe) synthesis

MIL-100(Fe) was synthesized using a hydrothermal method similar to the procedure described by Cheng et al. (2020), with some modifications. 0.6g Iron (III) chloride hexahydrate ($FeCl_3 \cdot 6H_2O$) and 035g trimesic acid (BTC) were dissolved in a 12.5ml of DI water. After 1 hour of stirring, the solution was transferred to a Teflon-lined autoclave and heated at 150°C for 12 hours. After cooling to room temperature, the resulting MIL-100(Fe) crystals were collected by filtration, washed with ethanol and distilled water, and dried under vacuum at 60°C [33].

2.2.2.3 Ni@MIL-100(Fe) synthesis

Initially, the synthesized Ni NPs were functionalized according to previous works, to enhance their compatibility with the MIL-100(Fe) framework [34]. In this process, 195 µL of mercaptoacetic acid (MAA) and 4.8 mL of ethanol were first combined. Next, 0.024 g of Ni NPs were added to the solution. The mixture was stirred at room temperature for 24 hours. The functionalized Ni NPs were then separated by centrifugation, washed with ethanol, and dried

under vacuum at 60°C. The functionalized Ni NPs and the precursors for MIL-100(Fe) ($FeCl_3 \cdot 6H_2O$ and BTC) were mixed in a solution of distilled water and ethanol. The mixture was transferred to a Teflon-lined autoclave and heated at 150°C for 24 hours. After cooling to room temperature, the resulting Ni@MIL-100(Fe) composite was collected by filtration, washed with ethanol and distilled water, and dried under vacuum at 60°C.

2.2.2.4 ZnO/MIL-100(Fe) Synthesis

ZnO/MIL-100(Fe) was synthesized by dissolving different amounts of commercially purchased ZnO NPs in 20ml DI water and adding it to the MIL-100(Fe) solution. The mixture was stirred for 60 minutes at room temperature. The subsequent process was similar to the MIL-100(Fe) synthesis. The mixture was transferred to a Teflon-lined autoclave and heated at 150°C for 12 hours. After cooling to room temperature, the resulting ZnO/MIL-100(Fe) composite was collected by filtration, washed with ethanol and distilled water, and dried under vacuum at 60°C. Composites with three different ZnO weight percentages were synthesized: ZnO0.5/MIL-100(Fe), ZnO0.1/MIL-100(Fe), and ZnO0.15/MIL-100(Fe). Following R6G degradation tests, the optimal composition was selected for synthesizing ZnO/Ni@MIL-100(Fe) composites to determine the best Ni loading percentage.

2.2.2.5 ZnO/Ni@MIL-100(Fe) Synthesis

ZnO/Ni@MIL-100(Fe) was synthesized by incorporating both ZnO and functionalized Ni NPs into the MIL-100(Fe) framework. A certain amount of ZnO NPs and different amount of functionalized Ni NPs were dissolved in 20 ml water separately. The functionalized Ni NPs were added first, followed by 1 hour of stirring to ensure homogeneous dispersion, and then the ZnO NPs were added and stirred similarly for another hour. The subsequent process followed the MIL-100(Fe) synthesis method. The mixture was transferred to a Teflon-lined autoclave and heated at 150°C for 12 hours. After cooling to room temperature, the resulting ZnO/Ni@MIL-100(Fe) composite was collected by filtration, washed with ethanol and distilled water, and dried under vacuum at 60°C. These synthesized materials were subsequently used in photocatalytic degradation experiments to evaluate their efficiency in degrading Rhodamine 6G (R6G) under UV and visible light conditions.

2.3 Characterization

Following the synthesis, a comprehensive characterization of ZnO NPs, Ni NPs, MIL-100(Fe), Ni@MIL-100(Fe), ZnO/Ni@MIL-100(Fe), and ZnO/MIL-100(Fe) nanoparticle samples was conducted. The XRD patterns were obtained with a Bruker D8 advance powder X-ray diffractometer using Cu Kα source (λ = 1.54178 Å). Morphological analysis was done by using FE-SEM (QuantaTM 250) Samples were deposited onto a silicon wafer and dried at 50°C. were observed using a Transmission Electron Microscope (TEM), with TEM mapping and EDS analysis providing insight into the element composition. The loaded ZnO and Ni NPs were quantified using Agilent Triple Quadrupole ICP-MS. The specific surface area and pore size distribution were determined through BET analysis using a Surface Area Analyzer Gemini VII 2390 Micromeritics instrument. Thermo-gravimetric analyses (TGA) of the synthesized composites were conducted using a Waters Discovery TGA 550 under atmospheric conditions, with a heating rate of 10°C min^{-1} up to 800°C. Fourier Transform Infrared Spectroscopy (FTIR, Nicolet Nexus 470, USA) was utilized to investigate chemical bond vibration of the synthesized materials. Absorbance spectra were measured with a METTLER TOLEDO EasyPlus visible spectrophotometer (Wavelength Range: 330 nm - 1,000 nm). Additionally, Inductively Coupled Plasma Mass Spectrometry (ICP-MS) analysis was conducted using a Agilent 8900 ICPQQQ to detect leaked elements from the catalyst in the final solution, providing insights into its stability over successive cycles of use. Nitrogen adsorption/desorption isotherms of the materials were obtained at 77 K by a Micromeritics Tristar II Plus surface area and porosity analyzer instrument equipped with MicroActive for TriStar II Plus Version 2.03 software for calculation and analysis. The Brunauer−Emmett−Teller (BET) method was used to determine the specific surface area of the samples. Total pore volume was calculated by N2 uptake at the relative pressure P/P0 = 0.99.

2.4 Adsorption studies

Adsorption capacity of the samples was tested using Rhodamine 6G (R6G) as the model dye in aqueous solution, representing a common pollutant in water remediation efforts. The adsorption experiments were carried out in a 50 ml beaker where 20 ml of a 4 ppm of R6G dye solution was prepared initially. 3 mg of each of the prepared samples were then added to the dye solution. The beaker was placed in a dark room to avoid photolysis reaction and is kept for

stirring. A known amount of sample was withdrawn every 10 min to monitor the absorbance using UV-Visible spectrophotometer.

2.5 Photocatalytic activity of the prepared samples

To assess the photodegradation of R6G over the synthesized catalyst, 3mg of catalyst was dispersed in a 20ml R6G solution (4ppm). Here, since the proposed composites can effectively adsorb the dye, this is crucial to attain adsorption equilibrium without oversaturating the active sites of the photocatalyst and limiting light penetration [21, 35]. Therefore, before starting the photocatalytic experiment the solution was stirred for 30min in dark. To establish a baseline understanding, a control experiment was initially conducted on the R6G solution without the presence of a photocatalyst under irradiation. This enabled the observation of the natural behavior of R6G, providing context for subsequent experiments. Following this, a series of experiments were conducted to evaluate the photodegradation efficiency of the composites under varying conditions. The solution was continuously stirred under either a UV irradiation (UVA Pencil light with a wavelength of 254 nm) or a visible light lamp (20 W TUNGSTEN HALOGEN lamp emitting light with a wavelength range of 360 nm to 2.4 μm) for 60 minutes. Subsequently, samples were collected at regular intervals (every 10 minutes), centrifuged, and the concentration of R6G in the supernatant was quantified using a METTLER TOLEDO EasyPlus visible spectrophotometer at the maximum absorbance intensity of the R6G positioned at 526 nm. These experiments formed the basis for assessing the photocatalytic activity of the composites under diverse experimental conditions, including variations in pH, type of light source, R6G and photocatalyst concentrations. Synthesis adjustments were made to optimize the composition of the catalysts for enhanced activity, involving varying the loading amounts of ZnO nanoparticles (NPs) and Ni NPs within the MIL-100(Fe) and Ni@MIL-100(Fe) frameworks. Additionally, scavenger experiments were conducted using $AgNO_3$, benzoquinone (BQ), and isopropyl alcohol (IPA) to elucidate the degradation mechanism, capturing specific reactive species such as superoxide radicals ($\bullet O^{2-}$), and hydroxyl (•OH) radicals. To evaluate the stability of the ZnO/MIL-100(Fe) and ZnO/Ni@MIL-100(Fe) photocatalysts, they were washed with acetone and ethanol, centrifuged at 4000 rpm for 5 minutes, and dried at 70°C for 12 hours to remove any remaining adsorbed substances on the composite surface. The recovered photocatalysts were then subjected to repeated cycles of R6G degradation to assess their reusability.

2.6 Results and Discussion

2.6.1 X-ray diffraction (XRD) analysis

The XRD patterns of the synthesized ZnO NPs show peaks consistent with those reported in the reference literature, and the sharpness of these peaks indicates good crystallinity of the samples (**Figure 1**a) [36]. For the Ni NPs, aside from the Ni NP peak at 51.8°, corresponding to the (200) plane of crystalline Ni species, peaks for NiO were observed at 37° and 43°, corresponding to the (100) and (111) planes, respectively, as supported by the literature [37, 38]. This oxidation of Ni NPs on the surface is common. Although the presence of a NiO layer on the Ni NPs was unintended, it is not detrimental; in fact, it can enhance the stability of the nanocomposite as NiO is a porous passive layer that can protect Ni NPs from corrosion [39]. All the synthesized nanocomposites display characteristic peaks of MIL-100(Fe) at 11.2°, 14.8°, 19.33°, and 27.8° [40]. After incorporating ZnO and Ni nanoparticles (NPs) into the MIL-100(Fe) framework, the PXRD pattern primarily shows the main peak of the MOF, indicating that its original crystalline structure is preserved. A small ZnO NP peak appears in ZnO/MIL-100(Fe) and ZnO/Ni@MIL-100(Fe) around 25°, attributed to (100), confirming the successful incorporation of ZnO NPs [41]. However, no peak for Ni NPs was detected possible due to the low amount of introduced Ni NPs. It can indicate a high dispersion of Ni NPs within the MIL-100(Fe) framework and their morphology as a core inside the MOFs, which aligns with the findings of literature [40].

2.6.2 FTIR analysis

The FTIR spectra of Ni NPs, ZnO NPs, Ni@MIL-100(Fe), ZnO/MIL-100(Fe), and ZnO/Ni@MIL-100(Fe) composites provide important insights into their chemical bonding and structural features. As shown in **Figure 1**b, Ni NPs exhibit characteristic peaks at various wavelengths, including 703.27 cm^{-1} (CH_2 bond), 1076.85 cm^{-1} (C-O bond stretching), 1396.66 cm^{-1} (C=C bond), 1576.55 cm^{-1} (N=N bond), 2943.16 cm^{-1} (CH_3 bond stretching), 3298.95 cm^{-1} (-OH bond stretching), a broad band at 3433 cm^{-1} (O–H stretching), and 626 cm^{-1} (Ni–O stretching) [42]. Similarly, the FTIR spectrum of ZnO nanoparticles shows absorption bands at 3400 cm^{-1} (O-H mode), 2300 cm^{-1} and 1400–1600 cm^{-1} (C=O stretching and CO_2 absorption), and 782 cm^{-1} (ZnO stretching), consistent with literature findings. For MIL-100(Fe), the peaks at 1643 cm^{-1}, 1577 cm^{-1}, and 1445 cm^{-1} (–O–C–O– group) and 3406 cm^{-1} (terminal –OH group on

Fe nodes) confirm the successful synthesis of the MOF. Additionally, Ni@MIL-100(Fe) exhibits combined features of both Ni and MIL-100(Fe), with notable Ni-O stretching at 952 cm^{-1} and 685 cm^{-1}. The ZnO/MIL-100(Fe) composite shows a peak at 450 cm^{-1} (Zn-O bond), along with peaks at 1149 cm^{-1} (C–C bonding), 1634 cm^{-1} (adsorbed CO_2 and moisture), and 3449 cm^{-1} (O–H stretching). Similarly, ZnO/Ni@MIL-100(Fe) displays peaks characteristic of both ZnO and Ni, including 952 cm^{-1} (Ni-O stretching) and 1047 cm^{-1} (Zn-O bond) [43-45]. These findings collectively confirm the successful synthesis and functionalization of the composites, preserving structural integrity and enhancing their photocatalytic potential.

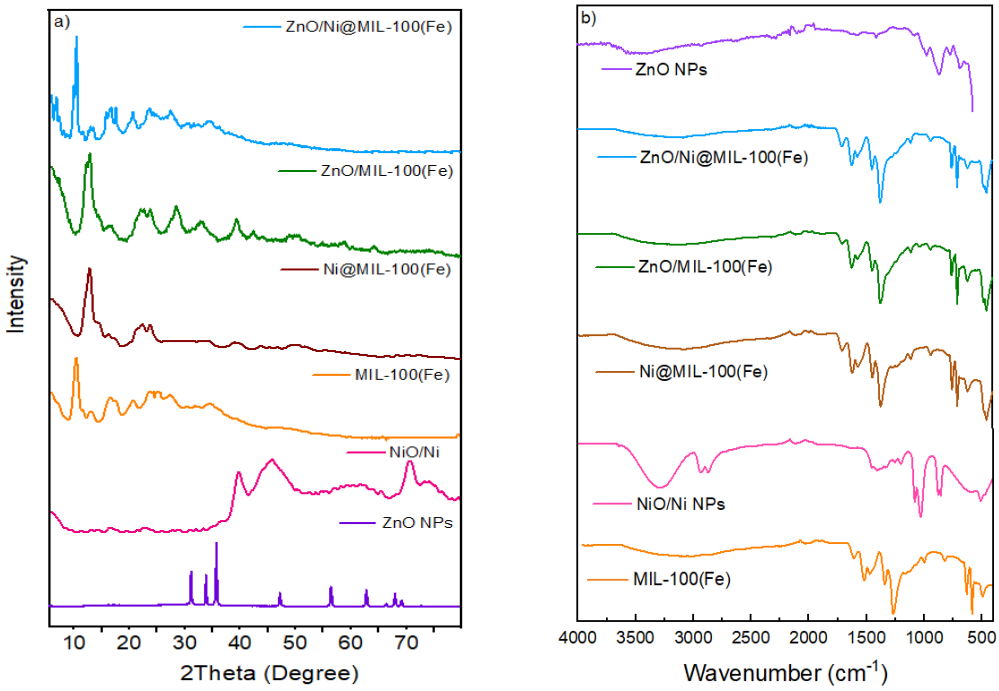

Figure 1. a) XRD diffraction pattern and b) FT-IR spectrum of Ni NPs, ZnO NPs, MIL-100(Fe), Ni@MIL-100(Fe) ZnO/MIL-100(Fe) and ZnO/Ni@MIL-100(Fe)

Figure S1 in the supporting information document shows the ICP-MS analysis results. As the results show the amount of loaded ZnO in ZnO/MIL-100(Fe) were around 5, 10, 15wt%. In case of ZnO/Ni@MIL-100(Fe) the weight percentage of the loaded Ni NPs were 0.1, 0.5 and 1. Notably, the observed weight percentages were found to be lower than the initial amounts of these materials used in the synthesis process. This difference is likely be attributed to the loss of some amount of ZnO and Ni nanoparticles during the washing stages and which did not effectively bond with the MIL-100(Fe) matrix.

2.6.4 Thermogravimetric analyzer (TGA)

Thermal stability of ZnO/MIL-100(Fe) and ZnO/Ni@MIL-100(Fe) was evaluated via thermogravimetric analysis (TGA) under N2 atmosphere from room temperature to 700°C, at a heating rate of 10°C/min. As the results indicate (Figure 2), both composites demonstrated excellent thermal stability, enduring temperatures up to 500°C without significant framework decomposition. Decomposition occurred in three stages, with an initial stage (25-200°C) showing approximately 16.12% weight loss for ZnO/MIL-100(Fe), attributed to the removal of absorbed water and guest solvent molecules from MIL-100(Fe) pores. ZnO/Ni@MIL-100(Fe) exhibited a comparable pattern but with a slightly lower weight loss of around 11.71%. In the second stage(200-500°C), both ZnO/MIL-100(Fe) and ZnO/Ni@MIL-100(Fe) composites underwent a notable weight loss. ZnO/MIL-100(Fe) experienced a weight loss of 51.34%, while ZnO/Ni@MIL-100(Fe) exhibited a slightly lower weight loss of 45.57%. This weight loss is primarily attributed to the structural collapse of MIL-100(Fe) as the ligand decomposes. In the third stage, occurring above 500°C, decomposition was attributed to the collapse and decomposition of MIL-100(Fe). This resulted in a weight loss of 46.04% for ZnO/MIL-100(Fe) and 35.08% for ZnO/Ni@MIL-100(Fe).

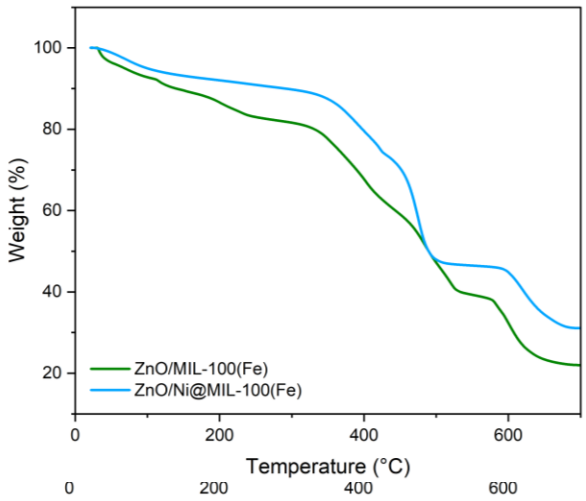

Figure 2. Thermal gravimetric analysis (TGA) curve of synthesized

2.6.5 Scanning Electron Microscopy (SEM)

Scanning electron microscopy (SEM**)** analysis was done on the as-prepared ZnO/MIL-100(Fe), Ni@MIL-100(Fe), and ZnO nanoparticles (NPs) samples. The dispersible spherical nanoparticles and nano-rods morphology of this material was shown in Figure S2. Figure S2

also demonstrate the narrow distribution of MIL-100(Fe) and Ni@MIL-100(Fe) particles that indicates despite of agglomeration a uniform dispersion of particles occurred throughout the sample. However, the specific morphology of the composites remains unclear. This finding is consistent across ZnO/MIL-100(Fe), ZnO/Ni@MIL-100(Fe), and Ni nanoparticles. The reason may stem from the particles' small size, hindering the resolution of distinct features, or from the presence of agglomerates that obscure the underlying structure. Consequently, TEM analysis was performed to gain further insight and clarify the structural characteristics of these materials.

2.6.6 TEM analysis

Figure 3a demonstrates the TEM image of Ni@MIL-100(Fe) reveal a core-shell morphology, wherein the core comprises Ni nanoparticles (NPs) surrounded by several MIL-100(Fe) NPs forming a shell structure. TEM results for ZnO/MIL-100(Fe) (**Figure 4**) suggest that mainly the spherical ZnO nanoparticles with around 50 nm or less particle size could successfully be decorated on the surface of MIL-100(Fe) and also enter the MOF channel. This preference can be attributed to the incompatibility of the nanorods' dimensions (100nm) with the particle size of the MOF (also approximately 100nm). Due to their similar sizes, the nanorods are less likely to effectively deposit on the MOF surface compared to the spherical nanoparticles. Therefore, the spherical nanoparticles, with potentially smaller effective sizes, would have a higher probability of interacting with and depositing to the MIL-100(Fe) and the larger ZnO NPs might have remained unreacted during the synthesis process and were subsequently washed away during the washing steps. This discrepancy may also account for the difference between the initial amount of ZnO added during synthesis and the loaded ZnO observed in ICP-MS results. In the case of ZnO-decorated Ni@MIL-100(Fe), the morphology exhibits a combination of the core-shell structure characteristic of Ni@MIL-100(Fe) and the deposition of ZnO nanoparticles (NPs) on the surface of the MOF (Figure 4b).

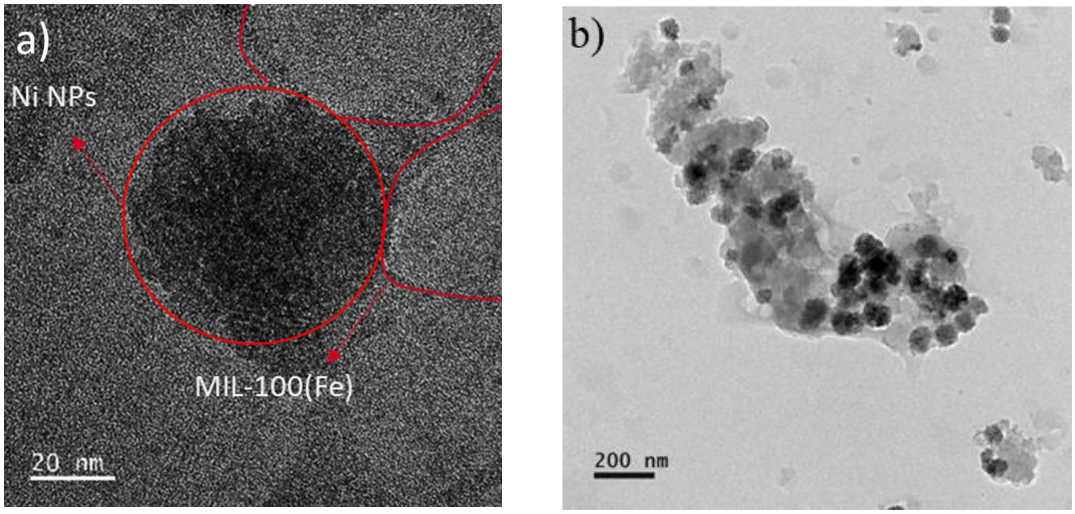

Figure 3. TEM image of a) Ni@MIL-100(Fe) and b) ZnO/MIL-100(Fe)

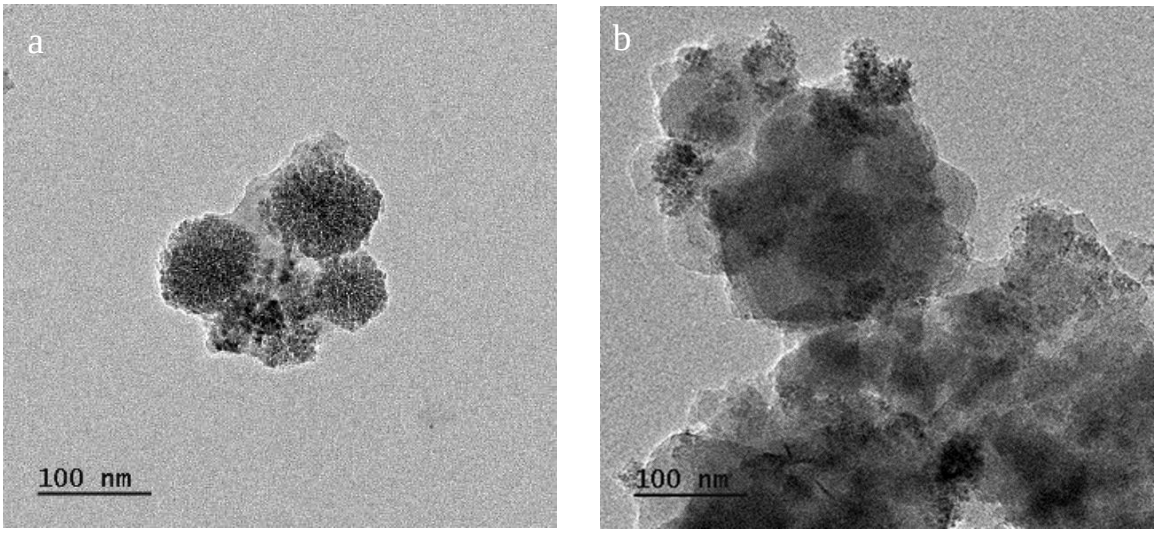

Figure 4. TEM image of a) ZnO/MIL-100(Fe) and b) ZnO/Ni@MIL-100(Fe)

Additionally, EDS TEM confirmed the presence of Zn, Ni, and Fe elements in the composites. There was also a Cu peak in the EDS results that came from the Cu grid. EDS mapping demonstrates a homogeneous and uniform dispersion of both ZnO NPs, along with Ni NPs, in ZnO/Ni@MIL-100(Fe) and ZnO nanoparticles (NPs) in ZnO/MIL-100(Fe) composites within the MIL-100(Fe) matrix (Figure 5).

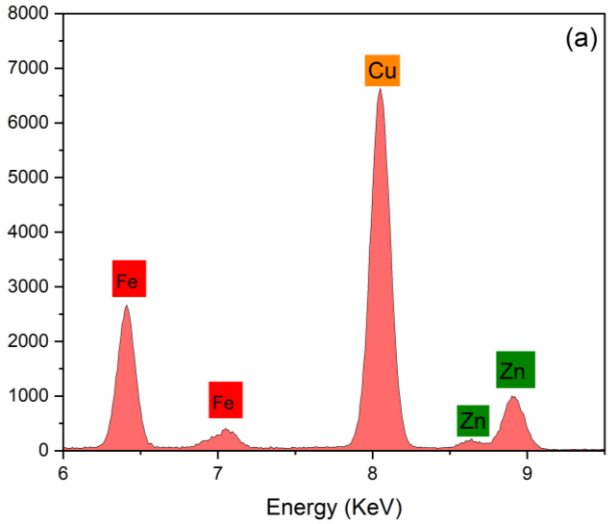
(a)
Cu
Fe
Fe
Zn
Zn
Energy (KeV)

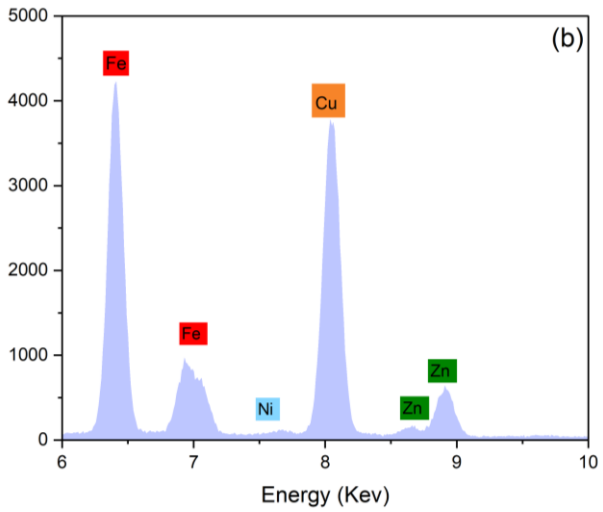
(b)
Fe
Cu
Fe
Ni
Zn
Zn
Energy (Kev)

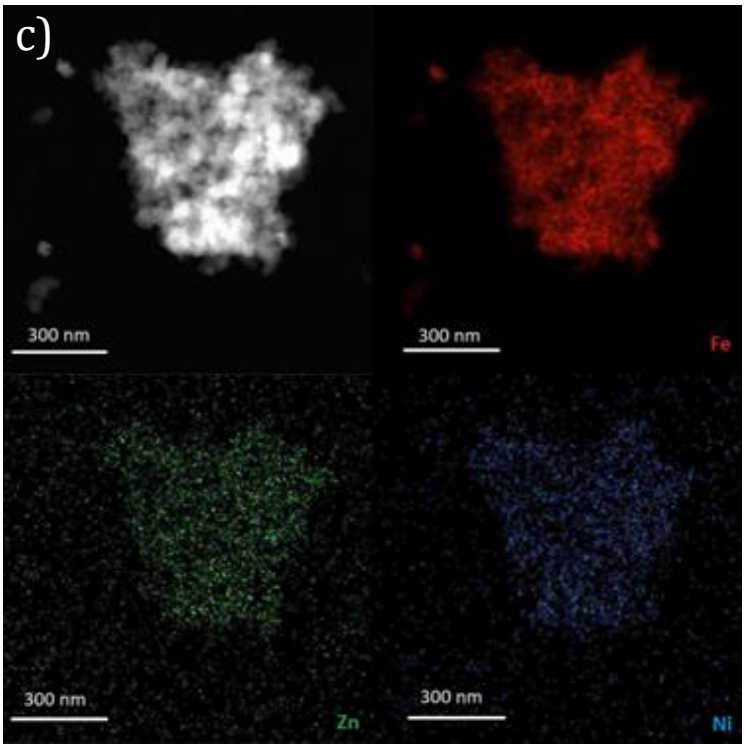
c)
300 nm
300 nm
Fe
300 nm
Zn
300 nm
Ni

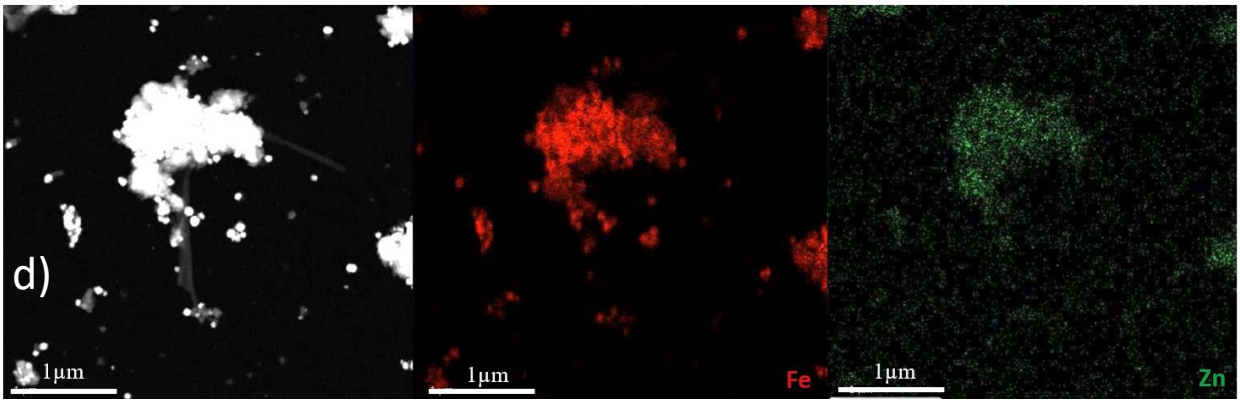

Figure 5. EDS TEM of a) ZnO/ MIL-100(Fe), b) ZnO/Ni@MIL-100(Fe) and EDS mapping of c) ZnO/ Ni@MIL-100(Fe), d) ZnO/MIL-100(Fe) and

2.6.7 UV-visible spectroscopy

The optical properties of the composite material were investigated using UV-visible spectroscopy, revealing a significant shift in the absorption peak from the UV range (around 220 nm) to the visible range (around 450 nm), compared to the absorption spectra of ZnO NPs Figure 6a. To determine the direct bandgap, Tauc's plot analysis was employed as follow [46]:

$$\alpha h\nu = B(h\nu - Eg)^2 \qquad 2$$

In this equation α represents the absorption coefficient at a given wavelength, hν denotes the energy of the incident photon, B stands for a proportionality constant, and Eg signifies the band gap energy of the semiconductor material. The direct band gap energy acquired by plotting of $(\alpha h\nu)^2$ against the energy of the absorbed light and extrapolating a tangential line from the linear area of the curve.

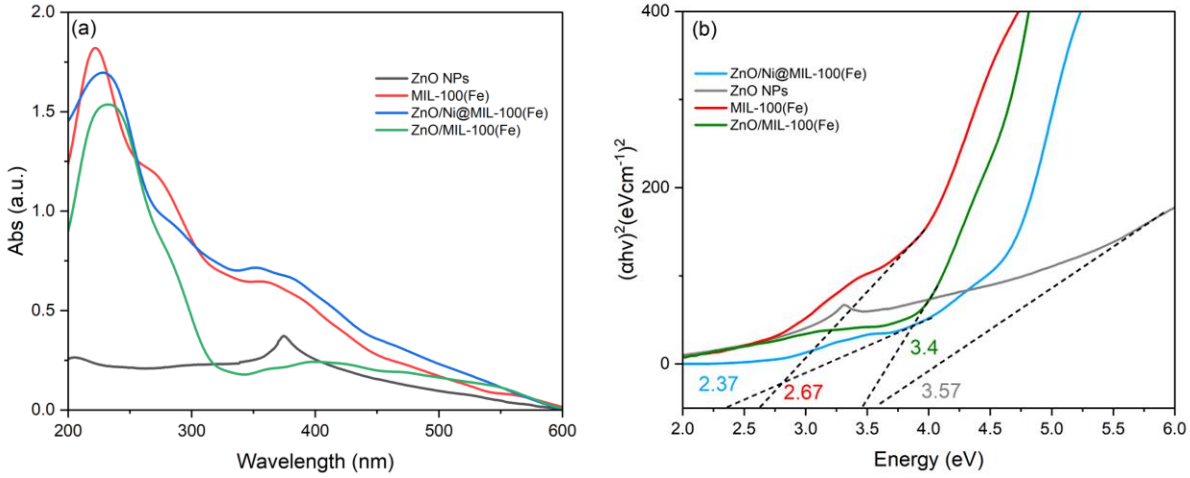

Figure 6. a) UV-VIS absorption spectrum and b) Direct bandgap energy of ZnO, MIL-100(Fe), ZnO/MIL-100(Fe) and ZnO/Ni@MIL-100(Fe).

This number was calculated to be 3.4 eV for ZnO/MIL-100(Fe) and 2.37 eV for ZnO/Ni@MIL-100(Fe), respectively Figure 6b. Therefore, both nanocomposites exhibit better light harnessing potential than ZnO NPs which possess a narrow bandgap and limited UV light absorption. This finding supports the shift observed in the absorption spectrum towards longer wavelengths, indicating enhanced absorption of visible light in Figure 6a. The shift in the ZnO/MIL-100(Fe) composite's absorption spectrum suggests significant modification in the material's optical behavior, likely driven by charge transfer phenomena facilitated by the defect-interface interaction between decorated ZnO nanoparticles and MIL-100(Fe) [47]. In comparison, the ZnO/Ni@MIL-100(Fe) composite exhibited not only an increase in absorption intensity but also a widening of the absorption range into the visible spectrum. This enhancements in optical properties attributes to the Local Surface Plasmon Resonance (LSPR) of Ni nanoparticles (NPs). LSPR in metal nanoparticles makes them efficient light absorbers and charge carriers, promoting electron transfer and catalytic processes. This alters energy levels and electronic states, shifting the band structure and effective bandgap of the composite material. [48, 49].

2.6.8 Textural Properties and BET Surface Area

The Brunauer-Emmett-Teller (BET) results presented in the Figure S3 indicate the nitrogen adsorption-desorption isotherms for MIL-100(Fe), ZnO15WT%/MIL-100(Fe), and ZnO15WT%/Ni@MIL-100(Fe). The isotherms for all samples exhibit a type IV shape, typical of mesoporous materials, with a noticeable hysteresis loop at higher relative pressures (P/P_0), suggesting the presence of mesopores [50].

Table 1. Textural properties of the ZnO, MIL-100(Fe), Ni NPs, ZnO/MIL-100(Fe) and ZnO/Ni@MIL-100(Fe)

Catalyst	S_{BET} ($m^2 g^{-1}$)	V_p ($cm^3 g^{-1}$)	D (nm)
ZnO NPs	13.5156	0.000963	12.4342
Ni NPs	34.8969	0.003334	10.7103
MIL-100(Fe)	39.9581	0.01144	5.8543
ZnO/MIL-100(Fe)	62.8604	0.008315	8.428
ZnO /Ni@MIL-100(Fe)	88.1968	0.013616	10.348

The N_2 adsorption-desorption analysis reveals significant improvements in the textural properties of the synthesized composites. As Table 1. indicates although MIL-100(Fe) was expected to have the highest surface area, but the BET results alone reveal a relatively low surface area of around 40 m^2/g due to agglomeration. However, by incorporation of ZnO nanoparticles into MIL-100(Fe) the BET surface area of the synthesized nanocomposite was 62.8 m^2/g, indicating that ZnO decoration prevents agglomeration and enhances surface area of both MIL-100(Fe) and ZnO NPs. Additionally, the average pore diameter increased from 5.8543 nm to 8.428 nm, suggesting some smaller ZnO NPs are embedded within the MIL-100(Fe) framework, as confirmed by the decreased pore volume [21]. A similar enhancement is observed in the ZnO/Ni@MIL-100(Fe) composite, where the S_{BET} further increased to 88.19 m^2/g. This significant rise is attributed to the core-shell morphology, where Ni nanoparticles form the core, and MIL-100(Fe) particles surround it, stabilizing the structure and preventing agglomeration. The slight increase in average pore diameter indicates some unfunctionalized Ni particles may occupy MIL-100(Fe) pores. The pore volume of ZnO/Ni@MIL-100(Fe) increased compared to both ZnO/MIL-100(Fe) and MIL-100(Fe), likely due to the formation of additional micropores through chemical bonding during MOF growth over Ni NPs [51]. Notably, the BET surface area of both ZnO/MIL-100(Fe) and ZnO/Ni@MIL-100(Fe) composites is larger than that of each individual component (ZnO, Ni NPs, and MIL-100(Fe)), demonstrating the effectiveness of the composite formation. Additionally, the BET analysis reveals that increasing the ZnO content in MIL-100(Fe) enhances both the surface area and pore volume while reducing the pore diameter, suggesting improved nanoparticle dispersion. Increasing the loading Ni to the ZnO/MIL-100(Fe) framework further increases the surface area and pore volume but results in even smaller pore diameters (Table S1). This trend is attributed to the nanoparticles filling larger pores. A higher Ni content leads to a significant rise in surface area and pore volume, with a marked decrease in pore size, indicating the nanoparticles' role in refining the pore structure through enhancing the agglomeration problem of the MIL-100(Fe) NPs [21, 52].

2.7 Results and Discussion

2.7.1 Adsorption studies

In the adsorption investigations, the removal efficiency, and the quantity of R6G dye absorbed per unit mass of the adsorbent at a given time (q_t in mg/g) was determined using the formulas below [33, 35]

$$\eta = \left(1 - \frac{C}{C_0}\right) \times 100 \qquad 3$$

$$q_t = \frac{(C_0 - C)}{m} \times V \qquad 4$$

Where C represent the dye concentration at time t [30], C_0 and C (in mg/l) represent the initial concentration and concentration of the R6G dye at time t respectively, V is the volume of the solution in liters, and m is the mass of the adsorbent in grams. Calibration curves were established to accurately measure dye concentrations, facilitating the evaluation of the degradation process. The adsorption findings reveal that after 60 minutes of stirring in the dark, 80.02% and 81.75% of the initial dye concentration was removed using ZnO/MIL-100(Fe) and ZnO /Ni@MIL-100(Fe) respectively, indicating the efficient adsorption ability of both synthesized nanocomposites. However, this percentage is significantly lower for MIL-100(Fe) and Ni@MIL-100(Fe), indicating the effect of BET surface area and pore volume. ZnO nanoparticles also exhibit very negligible adsorption, primarily due to their limited surface area.

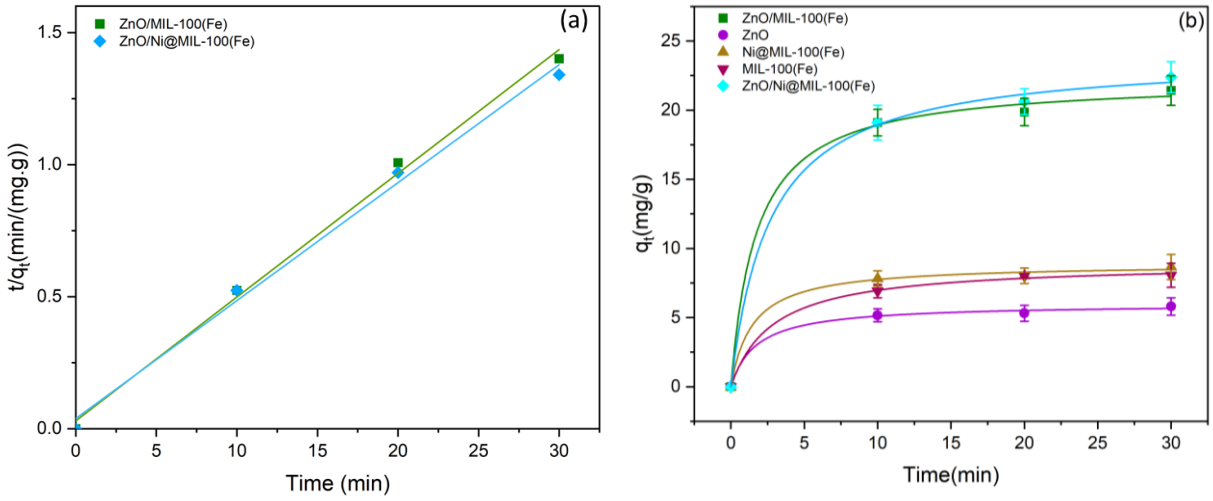

Figure 7. a) Plots of pseudo-second-order kinetics for R6G adsorption of the synthesized composites and b) Adsorption kinetics of ZnO/MIL-100(Fe), ZnO, Ni@MIL-100(Fe), MIL-100(Fe), and ZnO/Ni@MIL-100(Fe) photocatalysts for dye degradation over time.

Table 2.Adsorption capacity and regression coefficient of catalysts obtained from pseudo-second-order kinetics and removal efficiency.

Catalyst	$q_{t\ experimental}$ (mg/g)	$q_{t\ calculated}$ (mg/g)	R^2	Removal Efficiency (%)
ZnO NPs	5.8	5.767	0.99	19.46
MIL-100(Fe)	8.06	8.196	0.99	29.26
Ni@MIL-100(Fe)	8.66	8.622	0.99	32.12
ZnO/MIL-100(Fe)	21.42	21.73	0.99	80.02
ZnO /Ni@MIL-100(Fe)	22.01	26.31	0.99	81.75

Based on the experimental data collected, the theoretical models were developed to describe the adsorption kinetics of the synthesized samples. The pseudo-first order (PFO) (See Table S2 in the supporting information) and pseudo-second order (PSO) models were calculated and plotted for analysis using the formula below [35, 53-55].

PFO $$Ln\left(\frac{C_0}{C}\right) = kt \quad (5)$$

PSO $$\frac{t}{q_t} = \frac{1}{k_2 q_e^2} + \frac{1}{q_e} t \quad (6)$$

Where k is the apparent rate constant (min^{-1}), which corresponds to the slope when plotting -ln(C0/C) against time (t) and applying linear regression, k_2 is the second-order rate constant (g mg^{-1} min^{-1}) and qe is the amount of R6G adsorbed after reaching the equilibrium) [54]. Figure 7a displays the graphs for the pseudo-second-order models. The adsorption kinetic parameters were calculated using the equations from these theoretical models in Table S 3. The results demonstrated that the pseudo-second-order model exhibited a high correlation factor (0.99), indicating that this model fits the experimental data well and aligns with a chemisorption mechanism as the rate-controlling step [56]. The accuracy of the model was also confirmed as the qt value obtained from the PSO were close to the experimental qt. As Figure 7b demonstrates the adsorption capacity results correlate well with the BET surface area findings, indicating that higher surface areas lead to greater adsorption capacities. ZnO/Ni@MIL-100(Fe), with its high BET surface area and significant mesoporosity, demonstrated the best performance in terms of

adsorption capabilities and efficiency, followed closely by ZnO/MIL-100(Fe). MIL-100(Fe) enhanced the synthesized composites adsorption capabilities due to the synergistic interplay of multiple interactions and its structural properties. The benzene rings of trimesic acid (H_3BTC) in MIL-100(Fe) facilitate significant π-π stacking and hydrophobic interactions with the aromatic rings of the dyes, enhancing the adsorption affinity [57]. The negative surface charge of MIL-100(Fe) and ZnO NPs (around pH 5.5) strengthen electrostatic interactions with R6G which is a cationic dye [38, 58]. The presence of Ni nanoparticles enhances the adsorption properties through increasing the S_{BET} of the composites as the core Ni NPs caused a better arrangement in the MIL-100(Fe) NPs and address the agglomeration issue of the MIL100(Fe) leading to higher surface area. Since adsorption is a crucial step in photocatalytic reactions, these results confirm the potential of the composites as effective photocatalysts.

2.7.2 Photocatalytic activity of the prepared samples

The assessment of photocatalytic efficiency involved monitoring the intensity of the principal absorption peak of the R6G dye solution, situated at 526 nm. To analyze the influence of the photocatalyst, quantitative analyses were performed, including the determination of rate constants and the calculation of dye degradation percentages. These analyses allow for a comparative assessment of catalytic efficiency. The degradation efficiency was calculated using the formula written below:

$$\eta = 1 - C\mathcal{C}\square 0\square\square\square \times 100 \qquad 3.$$

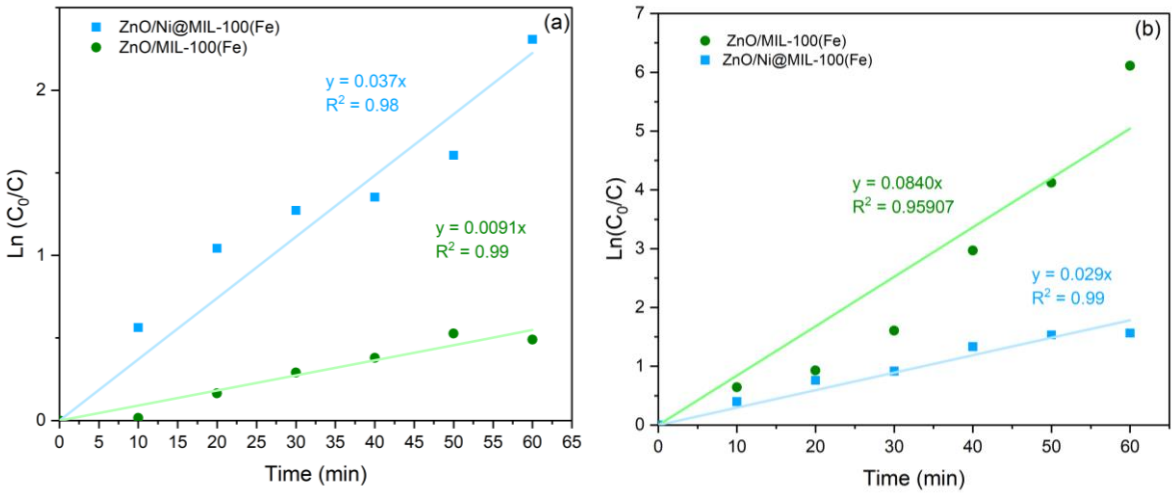

Figure 8. First-order linear transforms of Rhodamine 6G (R6G) degradation by ZnO/MIL-100(Fe), and ZnO/Ni@MIL-100(Fe) under a) visible light (20 W TUNGSTEN HALOGEN lamp emitting light with a wavelength range of 360 nm to 2.4 μm) and b) UV irradiation (Pencil UVC, wavelength = 254nm)

Table 3. Photocatalytic degradation rate constants (k), regression coefficients (R^2), and efficiency percentages of Rhodamine 6G (R6G) for various photocatalysts under visible and UV light irradiation.

Catalyst	Visible			UV		
	$k(min^{-1})$	R^2	Efficiency (%)	$k(min^{-1})$	R^2	Efficiency (%)
ZnO/MIL-100(Fe)	0.009	0.99	88	0.084	0.95	99
ZnO /Ni@MIL-100(Fe)	0.037	0.98	98	0.029	0.99	96
ZnO NPs	0.0059	0.92	50	0.0149	0.99	68
MIL-100(Fe)	0.0012	0.93	36	0.001	0.96	36
Ni@MIL-100(Fe)	0.0008	0.96	36	0.001	0.96	33

For fitting the dye degradation data, the pseudo-first-order kinetics equation was employed, and results were shown in Figure S4 [35, 53]. As Table 3. Shows the composite catalysts demonstrated significantly higher rate constants (k) for the photocatalytic degradation of Rhodamine 6G compared to MIL-100(Fe), ZnO NPs, and Ni@MIL-100(Fe). Under visible light, ZnO Ni@MIL-100(Fe) had the highest rate constant ($k = 0.037\ min^{-1}$). Under UV light, ZnO@MIL-100(Fe) exhibited the highest rate constant of $k = 0.084\ min^{-1}$, followed by ZnO Ni@MIL-100(Fe) at $k = 0.029\ min^{-1}$. The enhanced performance of these composites is due to the interaction between Ni NPs and MIL-100(Fe), which facilitates the migration of photogenerated charges, thus boosting photocatalytic efficiency [50]. Additionally, the synergy between ZnO and MIL-100(Fe) improves electron-hole recombination prevention, and the high surface area of these composites provides more active sites for reactions, leading to more effective photocatalytic degradation of Rhodamine 6G.

2.7.1 Key Factors Influencing Photocatalytic Efficiency

2.7.1.1 Light Source Effect

In order to investigate the efficiency of the photocatalyst under visible (20 W TUNGSTEN HALOGEN lamp emitting light with a wavelength range of 360 nm to 2.4 μm) and UV (Pencil UVC, wavelength = 254nm) light sources, the light source effect was conducted. Figure S5. shows the UV–vis absorption spectra of Rh6G solution during the photodegradation under UV and visible light source. Among all the photocatalysts ZnO/Ni@MIL-100(Fe) showed

the highest degradation efficiency, reaching nearly 98% within 60 minutes under visible irradiation. As Figure 9. shows a significant increase in the degradation efficiency of R6G immediately after the transition from dark to visible light occurs which highlights the strong photocatalytic activity of this composite. ZnO/MIL-100(Fe) shows a degradation efficiency of around 88% under visible light as it possesses a wider bandgap than ZnO/Ni@MIL-100(Fe) and consequently limits in terms of absorbing light with longer wavelength. This highlights the effective role of Ni NPs in the composite which leads to a better light absorption due to LSPR phenomenon as discussed earlier. ZnO nanoparticles showed moderate efficiency at around 50% under visible irradiation, limited by their wide bandgap, surface area constraints, and rapid electron-hole recombination. MIL-100(Fe) and Ni@MIL-100(Fe) had the lowest efficiencies, around 20-25%, with minimal improvement under visible light, due to low surface area from agglomeration and rapid electron-hole recombination. Under UV irradiation, both ZnO/MIL-100(Fe) and ZnO/Ni@MIL-100(Fe) emerged as highly effective photocatalysts, achieving degradation rates of approximately 99% and 98%, respectively. This enhanced efficiency is attributed to their effective adsorption properties and photocatalytic reactions.

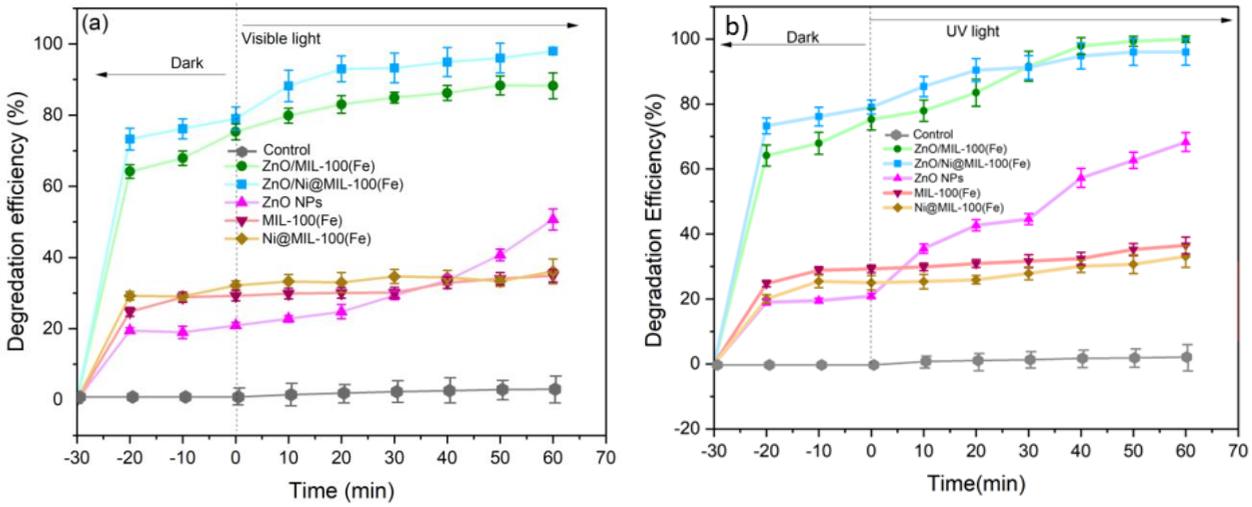

Figure 9. R6G Photodegradation in presence of different photocatalysts under a) visible and b) UV irradiation (C_o = 4 ppm and 150 ppm catalyst dose, pH = 6.5)

Under UV light, ZnO/MIL-100(Fe) exhibited the highest degradation efficiency, reaching 99% within 60 minutes. This outstanding performance highlights the synergistic effect between ZnO and MIL-100(Fe), which likely enhances charge separation and transfer, leading to superior

photocatalytic activity. ZnO/Ni@MIL-100(Fe) followed closely, with a degradation efficiency of approximately 96%. ZnO nanoparticles alone achieved around 75% degradation efficiency, highlighting the intrinsic photocatalytic activity of ZnO under UV light. In contrast, MIL-100(Fe) and Ni@MIL-100(Fe) showed lower efficiencies, around 35% and 25% respectively. Due to obtained results, all the further experiments were conducted under UV for ZnO/MIL-100(Fe) and under visible light for ZnO/Ni@MIL-100(Fe) to achieve the highest efficiency. Table S4 which has been shown in the supporting information provides a detailed comparison of the photocatalytic degradation efficiencies of Rhodamine 6G (Rh6G) across various catalyst systems, including the newly synthesized ZnO/Ni@MIL-100(Fe) and ZnO/MIL-100(Fe). The results underscore the competitive performance of these new composites, with both showing significantly high degradation efficiencies under different light sources. These findings suggest that ZnO/Ni@MIL-100(Fe) and ZnO/MIL-100(Fe) are highly effective in degrading Rh6G, positioning them as promising candidates for practical photocatalytic applications.

2.7.1.2 Effect of Loaded ZnO and Ni NPs

Figure 10a. shows the effect of increasing ZnO NPs amount within the composites. As the plot shows increasing ZnO NPs content enhances the degradation efficiency of R6G. Specifically, loading 15wt% of ZnO results in the highest degradation, indicating that more ZnO provides additional active sites and improves charge separation.

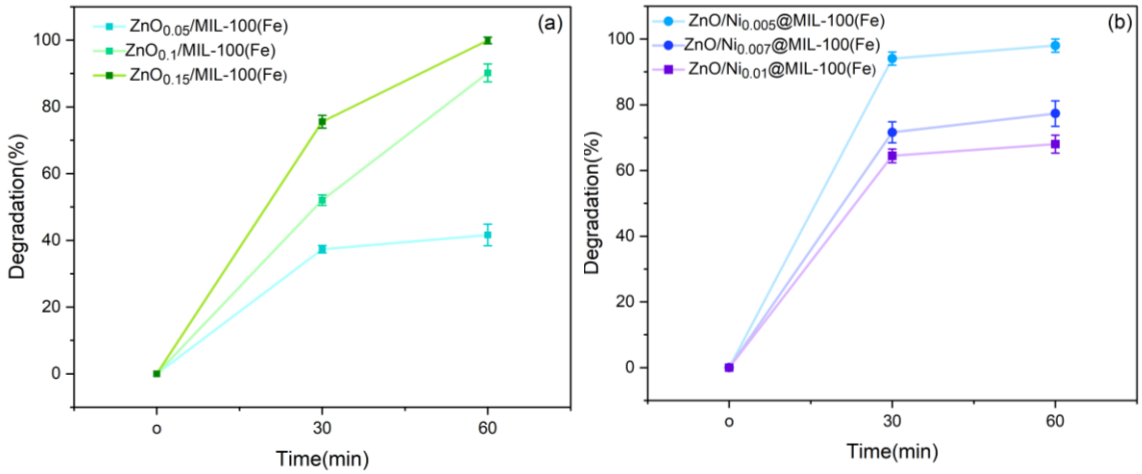

Figure 10. The effect of loading a) ZnO NPs and b) Ni NPs on the R6G degradation

Figure 10b. demonstrates that increasing the amount of Ni NPs in ZnO/MIL-100(Fe) composites also boost degradation efficiency. The optimal Ni loading found to be 0.5 wt% in ZnO/Ni@MIL-100(Fe) as it achieves the highest degradation efficiency, whereas higher Ni loadings reduce efficiency likely due to potential agglomeration and blockage of active sites and decreasing the pore diameter to 2nm which restrict the diffusion of R6G molecules into the adsorbent material. Therefore, all the further experiments have been conducted with $ZnO_{0.15}$/MIL-100(Fe) and $ZnO_{0.15}/Ni_{0.005}$@MIL-100(Fe)

2.7.1.3 Effect of pH

For photocatalytic dye decolorization, pH plays a crucial role, as it can significantly impact dye reaction rates in various ways. Many studies have explored how pH affects the photocatalytic degradation of dyes. Overall, two main factors need to be considered: firstly, industrial pollutants typically have non-neutral pH levels, and secondly, the pH of the reaction mixture affects the surface charge properties of the photocatalysts. To find the effect of pH on the R6G degradation over the synthesized catalysts, the degradation of Rhodamine 6G (R6G) was investigated in various pH ranges from 2-11.5 using NaOH and H_2SO_4 solution.

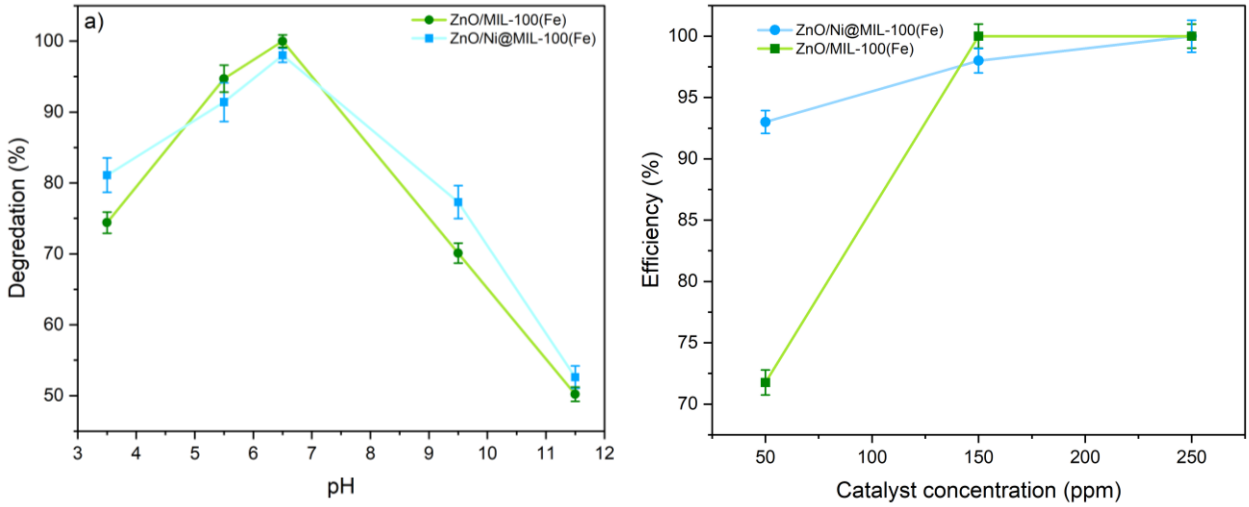

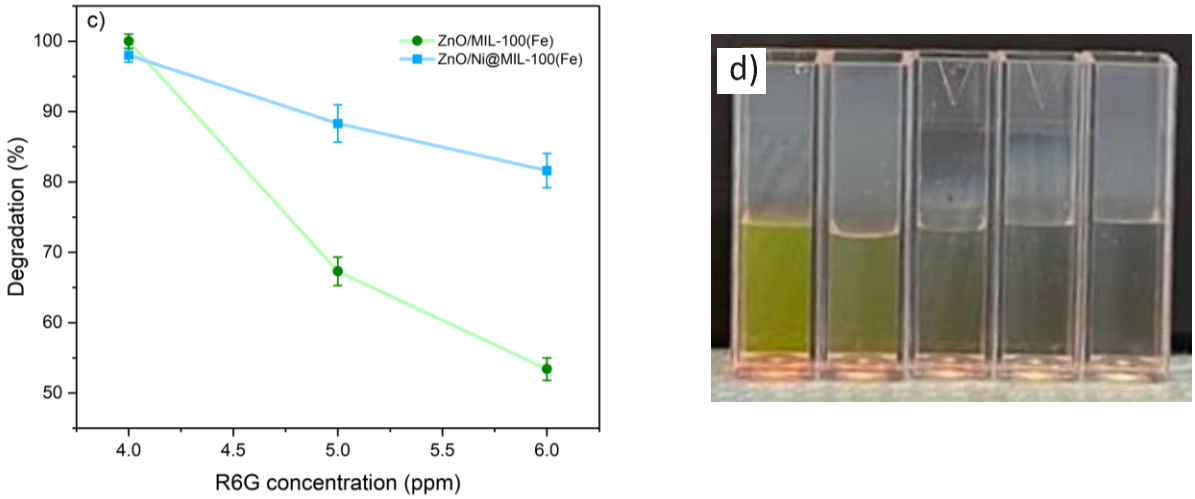

Figure 11. (a) Degradation efficiency of R6G at different pH levels for ZnO/MIL-100(Fe) and ZnO/Ni@MIL-100(Fe) under UV and visible light irradiation. (b) Photocatalytic efficiency of ZnO/MIL-100(Fe) and ZnO/Ni@MIL-100(Fe) as a function of catalyst concentration under UV and visible light irradiation. (c) Degradation efficiency of R6G at varying R6G concentrations for ZnO/MIL-100(Fe) and ZnO/Ni@MIL-100(Fe) under UV and visible light irradiation. (d) R6G discoloration by ZnO/Ni@MIL-100(Fe) photocatalyst, from left to right: 0 min, after 30 min of stirring in the dark, and after 20, 40, and 60 min under visible light irradiation.

Figure 11a. indicates that at pH levels lower than 6.5, the efficiency decreases. This is due to the amphoteric nature of ZnO and the fact that ZnO surfaces become positively charged below the point of zero charge (PZC), which is 5.5 in our case. Additionally, as indicated in previous works, when the pH increases from 1 to 5, the zeta potential of MIL-100(Fe) becomes more negative, enhancing the adsorption of R6G [38]. At high pH, the ZnO surface is negatively charged and attracts R6G. However, the efficiency also decreases at pH higher 6.5, which can be attributed to the excess hydroxyl ions (OH^-) present that compete with R6G for adsorption sites on the ZnO surface and the less negative zeta potential of MIL-100(Fe) at pH levels higher than 8. Moreover, the MIL-100(Fe) structure degrades at very low pH due to protonation and at high pH due to deprotonation. Therefore, optimal degradation occurs near neutral pH, where the optimal surface negative charge on the nanocomposite maximizes adsorption and MIL-100(Fe) maintains structural integrity, providing the best conditions for photocatalytic efficiency [38, 41, 59]. Therefore, all the other experiments were conducted at pH=6.5.

2.7.2 Effect of photocatalyst concentration

The concentration of the photocatalyst significantly affects dye degradation. As the amount of photocatalyst increases, the photodegradation of dye also increases due to the higher number of active sites available on the catalyst surface. This increase in active sites enhances the generation of hydroxyl radicals (•OH), which are crucial for dye discoloration. However, beyond a certain concentration limit, the solution becomes cloudy, obstructing UV radiation and reducing the percentage of dye decolorization [60]. Here the photocatalyst concentration for maximum efficiency was investigated. **Figure 11**b. illustrates the photocatalytic degradation efficiency of ZnO/Ni@MIL-100(Fe) and ZnO/MIL-100(Fe) composites at different concentrations (50 ppm, 150 ppm, and 250 ppm). ZnO/MIL-100(Fe) achieved 99% degradation efficiency at 150 ppm under UV light, likely due to a higher reaction rate compared to ZnO/Ni@MIL-100(Fe), which reached 98% efficiency at 150 ppm under visible light. Additionally, at 50 ppm, ZnO/Ni@MIL-100(Fe) degraded more R6G than ZnO/MIL-100(Fe), likely due to its higher adsorption capacity, which results from its larger surface area, enhanced electron-hole separation, and more active sites, enabling effective photocatalysis at lower photocatalyst concentrations. Conversely, ZnO/MIL-100(Fe) has a more limited adsorption capacity and requires higher concentrations to provide sufficient active sites for effective degradation. Considering cost-effectiveness, the ideal concentration for ZnO/Ni@MIL-100(Fe) was identified as 150 ppm, as its 98% degradation is nearly as effective as 99%, despite complete degradation being achievable at 320 ppm. As will be discussed further, the catalysts are stable and can be reused, so using a higher amount of photocatalyst is not necessarily problematic. However, for better comparison between ZnO/MIL-100(Fe) and ZnO/Ni@MIL-100(Fe) in further experiments, a consistent photocatalyst concentration of 150 ppm was used. Thus, all experiments were conducted with 150 ppm of the catalyst.

2.7.3 Effect of dye concentration

With increasing dye concentration, more organic material adsorbs onto the photocatalyst's surface, which reduces photon penetration and the production of hydroxyl and superoxide ions, resulting in lower degradation percentages [60]. As shown in **Figure 11**c. ZnO/Ni@MIL-100(Fe) consistently shows higher degradation rates across all concentrations. According to BET analysis, ZnO/Ni@MIL-100(Fe) has a larger pore volume and surface area, enhancing its adsorption capacity. This increased adsorption provides more active sites, maintaining higher

catalytic activity even at elevated R6G concentrations. Consequently, ZnO/Ni@MIL-100(Fe) resists saturation more effectively than ZnO/MIL-100(Fe), resulting in superior degradation performance.

2.7.4 Proposal for a photo-degradation mechanism

In order to provide insights into the reaction pathways. Different types of scavengers were used to investigate the impact of reactive oxygen species (ROS) on the degradation percentages of Rhodamine 6G (R6G) using ZnO/Ni@MIL-100(Fe) and ZnO/MIL-100(Fe) photocatalysts. As Figure 12a. shows, Benzoquinone (BQ), which quenches superoxide anions ($O_2^{\bullet -}$), slightly reduces degradation to 91.4% for ZnO/Ni@MIL-100(Fe) and 90.18% for ZnO/MIL-100(Fe), indicating the minor and negligible role of superoxide anions. Silver nitrate ($AgNO_3$), which traps electrons, decreases degradation to 86.2% and 78.75%, respectively, showing the role of electrons in the degradation reaction of R6G. Isopropanol (IPA), a scavenger for hydroxyl radicals (•OH), dramatically drops degradation to 67.3% and 56.4%, implying the crucial role of hydroxyl radicals. Overall, in this work, the proposed photo-degradation pathway is based on generating $O_2^{\bullet -}$ and •OH by reducing O_2 and oxidizing water respectively. The produced $O_2^{\bullet -}$, and •OH, then degrade R6G. Under UV light, ZnO/MIL-100(Fe) generates electron-hole pairs, forming $O_2^{\bullet -}$ and •OH that degrade R6G.

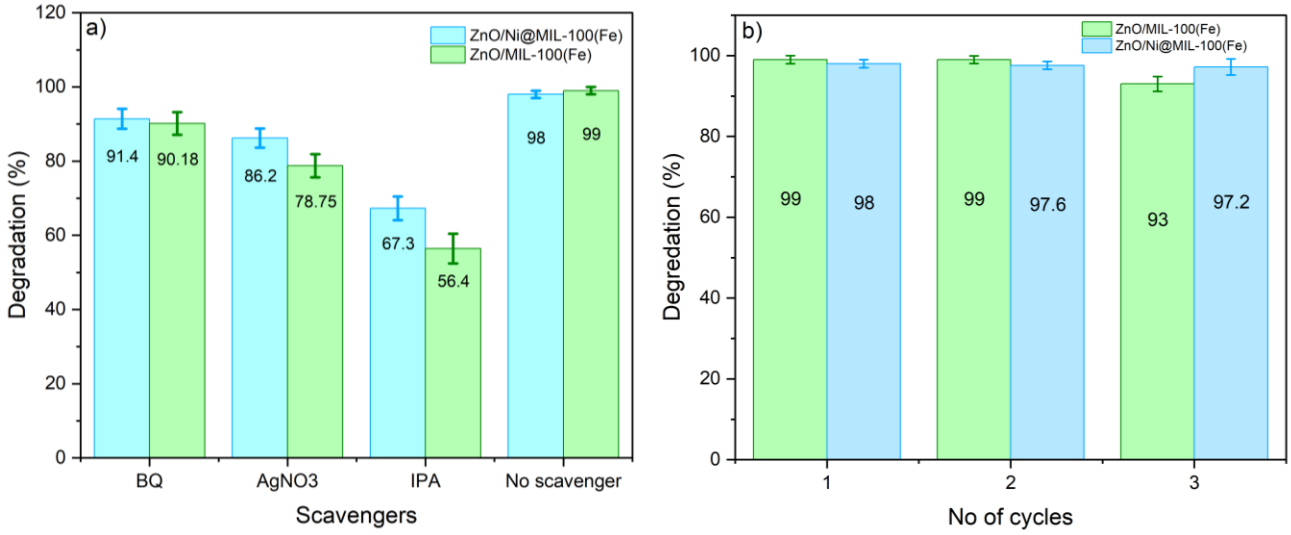

Figure 12. a) Photo-degradation of R6G in the presence of different scavengers for ZnO/MIL-100(Fe), ZnO/Ni@MIL-100(Fe) catalyst

The possible main reactions occurring during the photodegradation is explained below [61]:

$$ZnO/MIL100(Fe)\ or\ ZnO/Ni@MIL-100(Fe) + h\nu \rightarrow e_{CB}^{-} + h_{VB}^{+} \quad (7)$$

$$O_2 + e_{CB}^{-} \rightarrow O_2^{\bullet -} \quad (8)$$

$$H_2O + h_{VB}^{+} \rightarrow \bullet OH + H^{+} \quad (9)$$

$$OH^{-} + h_{VB}^{+} \rightarrow \bullet OH \quad (10)$$

$$O_2^{\bullet -}/\bullet OH + R6G \rightarrow CO_2 + H_2O \quad (11)$$

2.7.5 Catalyst Recovery

Figure 12b, illustrates the degradation efficiency of the synthesized nanocomposites over three cycles. ZnO/MIL-100(Fe) maintained stable performance during the first two cycles, but its efficiency decreased to 93% by the third cycle. This decline suggests a potential loss of activity, possibly due to material loss during the washing process, catalyst deactivation, or the photocorrosion of ZnO under prolonged UV exposure. In contrast, ZnO/Ni@MIL-100(Fe) demonstrated excellent stability across all cycles, with only a slight decrease likely due to material loss. Therefore, ZnO/Ni@MIL-100(Fe) proves to be a more stable catalyst. The incorporation of a small amount of Ni nanoparticles enhances the overall stability of the composite, enabling it to function effectively under visible light and reducing the likelihood of ZnO photocorrosion. Additionally, the NiO layer covering the Ni nanoparticles acts as a passive protective barrier, preventing the corrosion of Ni nanoparticles by R6G.

2.8 Conclusion

This study explored the photocatalytic degradation efficiencies of MIL-100(Fe)-based composites under both UV and visible light. The synthesized ZnO/MIL-100(Fe) and ZnO/Ni@MIL-100(Fe) photocatalysts were evaluated for their ability to degrade Rhodamine 6G (R6G). Under UV light, ZnO/MIL-100(Fe) achieved complete degradation within 60 minutes, showcasing the strong synergistic effect between ZnO and MIL-100(Fe) in enhancing charge separation and transfer. ZnO/Ni@MIL-100(Fe) followed closely with a 96% degradation efficiency, emphasizing the role of Ni nanoparticles in improving photocatalytic performance through enhanced adsorption kinetics and charge carrier dynamics. Under visible light, ZnO/Ni@MIL-100(Fe) demonstrated superior efficiency, achieving nearly 98% degradation within 60 minutes due to the synergistic effects of enhanced light absorption and specific chemical interactions between Ni nanoparticles and R6G molecules. In comparison, ZnO/MIL-100(Fe) showed an 88% degradation efficiency. Both composites exhibited significantly higher

efficiencies compared to ZnO NPs, MIL-100(Fe), and Ni@MIL-100(Fe) alone, and demonstrated excellent reusability, maintaining high degradation efficiencies over multiple cycles. This study highlights the potential of ZnO/MIL-100(Fe) and ZnO/Ni@MIL-100(Fe) composites for practical applications in environmental remediation, driven by their enhanced photocatalytic activities, adsorption properties, and reusability.

Chapter 3: Conclusion

In this study, MIL-100(Fe)-based composites, specifically ZnO/MIL-100(Fe) and ZnO/Ni@MIL-100(Fe), were synthesized and evaluated for their photocatalytic degradation of Rhodamine 6G (R6G) under both UV and visible light. The primary goal was to enhance the efficiency of dye degradation using novel composite materials that offer improved surface area, charge separation, and overall photocatalytic performance. Various factors influencing photocatalytic performance, such as pH, catalyst concentration, dye concentration, and light source, were thoroughly investigated to optimize degradation efficiency. Mechanistic studies were also conducted to understand the generation of reactive oxygen species (ROS) and the role of different components in the degradation process. The synthesized composites were assessed for their reusability to determine their practical application potential. Therefore, the designed questions mentioned in the "Research Question" section were answered and the finding of the project can be listed as below:

- **Photocatalytic Performance under UV Light:**
  - ZnO/MIL-100(Fe) achieved complete degradation of R6G within 60 minutes.
  - ZnO/Ni@MIL-100(Fe) exhibited a 96% degradation rate.
  - The exceptional performance is attributed to improved charge separation and transfer processes.
- **Photocatalytic Performance under Visible Light:**
  - ZnO/Ni@MIL-100(Fe) achieved nearly 98% degradation of R6G within 60 minutes.
  - ZnO/MIL-100(Fe) showed an 88% degradation efficiency.
  - The superior performance of ZnO/Ni@MIL-100(Fe) is due to enhanced light absorption, efficient electron scavenging, and specific chemical interactions.
- **Comparative Efficiency:**
  - Both composites significantly outperformed ZnO nanoparticles, MIL-100(Fe), and Ni@MIL-100(Fe) alone.
  - The results highlight the importance of combining metal-organic frameworks (MOFs) with semiconductor nanoparticles.
- **Reusability:**

- Both composites maintained high degradation efficiencies over multiple cycles, indicating excellent reusability.

- **Optimal Conditions:**
  - Near-neutral pH levels were optimal for performance.
  - Ideal catalyst concentration was determined to be 150 ppm.
  - The composites were effective across a range of dye concentrations.
- **Mechanistic Insights:**
  - Photocatalytic degradation involved the generation of ROS, with hydroxyl radicals playing a dominant role.
  - Ni nanoparticles in ZnO/Ni@MIL-100(Fe) enhanced ROS generation, leading to improved degradation rates.

Overall, ZnO/MIL-100(Fe) and ZnO/Ni@MIL-100(Fe) composites are highly efficient and cost-effective photocatalysts for organic dye degradation. As they show promise for practical applications in environmental remediation, particularly in treating dye-contaminated wastewater. Thus, future work can focus on investigating the potential of these composites in different applications such as degradation of various types of waste dye or using it as a photocatalyst for CO_2 conversion processes. Additionally, the effectiveness of the synthesized composites can be assessed under natural sunlight. Finally, optimizing the synthesis process of ZnO and MIL-100 nanoparticles, in order to obtain smaller particle size and less agglomerated product will be an effective way to enhance the overall activity of the synthesized samples.

References

1. Kant, R., *Textile dyeing industry an environmental hazard.* 2011.
2. Tomar, T., et al., *Bioremediation of synthetic dyes from wastewater by using microbial nanocomposites: An emerging field for water pollution management.* Biocatalysis and Agricultural Biotechnology, 2023: p. 102767.
3. Berradi, M., et al., *Textile finishing dyes and their impact on aquatic environs.* Heliyon, 2019. **5**(11).
4. Nidheesh, P., M. Zhou, and M.A. Oturan, *An overview on the removal of synthetic dyes from water by electrochemical advanced oxidation processes.* Chemosphere, 2018. **197**: p. 210-227.
5. Rafaqat, S., et al., *Recent progress in treatment of dyes wastewater using microbial-electro-Fenton technology.* RSC advances, 2022. **12**(27): p. 17104-17137.
6. Kumari, H., et al., *A review on photocatalysis used for wastewater treatment: dye degradation.* Water, Air, & Soil Pollution, 2023. **234**(6): p. 349.
7. Othman, Z., et al., *Efficient photocatalytic degradation of organic dyes by AgNPs/TiO2/Ti3C2T x MXene composites under UV and solar light.* ACS omega, 2021. **6**(49): p. 33325-33338.
8. Hassaan, M.A., et al., *Principles of photocatalysts and their different applications: a review.* Topics in Current Chemistry, 2023. **381**(6): p. 31.
9. Saravanan, R., F. Gracia, and A. Stephen, *Basic principles, mechanism, and challenges of photocatalysis.* Nanocomposites for visible light-induced photocatalysis, 2017: p. 19-40.
10. Umar, M. and H.A. Aziz, *Photocatalytic degradation of organic pollutants in water.* Organic pollutants-monitoring, risk and treatment, 2013. **8**: p. 196-197.
11. Aziri, S., et al., *Screening and optimization of the most influencing factors during the photodegradation of Rhodamine B by zinc oxide photocatalyst: application of Plackett–Burman and central composite designs.* Reaction Kinetics, Mechanisms and Catalysis, 2024.
12. Chiu, Y.-H., et al., *Mechanistic insights into photodegradation of organic dyes using heterostructure photocatalysts.* Catalysts, 2019. **9**(5): p. 430.
13. Hashimoto, K., H. Irie, and A. Fujishima, *TiO2 photocatalysis: a historical overview and future prospects.* Japanese journal of applied physics, 2005. **44**(12R): p. 8269.
14. Armaković, S.J., M.M. Savanović, and S. Armaković, *Titanium dioxide as the most used photocatalyst for water purification: An overview.* Catalysts, 2022. **13**(1): p. 26.
15. Sakar, M., R. Mithun Prakash, and T.-O. Do, *Insights into the TiO2-based photocatalytic systems and their mechanisms.* Catalysts, 2019. **9**(8): p. 680.
16. Raha, S. and M. Ahmaruzzaman, *ZnO nanostructured materials and their potential applications: progress, challenges and perspectives.* Nanoscale Advances, 2022. **4**(8): p. 1868-1925.
17. Porrawatkul, P., et al., *Morphology-dependent photocatalytic performance of ZnO nanostructures in organic dye and antibiotic degradation.* International Journal of Environmental Science and Technology, 2024: p. 1-18.
18. Sunaina, et al., *Surface photosensitization of ZnO by ZnS to enhance the photodegradation efficiency for organic pollutants.* SN Applied Sciences, 2021. **3**(7): p. 689.

19. Laurier, K.G., et al., *Iron (III)-based metal–organic frameworks as visible light photocatalysts.* Journal of the American Chemical Society, 2013. **135**(39): p. 14488-14491.
20. Duan, S., et al., *HF-free synthesis of nanoscale metal–organic framework NMIL-100 (Fe) as an efficient dye adsorbent.* ACS Sustainable Chemistry & Engineering, 2016. **4**(6): p. 3368-3378.
21. Amdeha, E. and R.S. Mohamed, *A green synthesized recyclable ZnO/MIL-101 (Fe) for Rhodamine B dye removal via adsorption and photo-degradation under UV and visible light irradiation.* Environmental Technology, 2021. **42**(6): p. 842-859.
22. Kaur, R., et al., *Efficient photocatalytic degradation of rhodamine 6G with a quantum dot-metal organic framework nanocomposite.* Chemosphere, 2016. **154**: p. 620-627.
23. Wen, J., Y. Fang, and G. Zeng, *Progress and prospect of adsorptive removal of heavy metal ions from aqueous solution using metal–organic frameworks: a review of studies from the last decade.* Chemosphere, 2018. **201**: p. 627-643.
24. Gao, G., et al., *UiO-66 (Zr) as sorbent for porous membrane protected micro-solid-phase extraction androgens and progestogens in environmental water samples coupled with LC-MS/MS analysis: The application of experimental and molecular simulation method.* Microchemical Journal, 2019. **146**: p. 126-133.
25. Bezverkhyy, I., G. Weber, and J.-P. Bellat, *Degradation of fluoride-free MIL-100 (Fe) and MIL-53 (Fe) in water: Effect of temperature and pH.* Microporous and Mesoporous Materials, 2016. **219**: p. 117-124.
26. Dhakshinamoorthy, A., et al., *Comparison of porous iron trimesates basolite F300 and MIL-100 (Fe) as heterogeneous catalysts for lewis acid and oxidation reactions: roles of structural defects and stability.* Acs Catalysis, 2012. **2**(10): p. 2060-2065.
27. Ye, Q., et al., *Photoinduced Dynamic Ligation in Metal–Organic Frameworks.* Journal of the American Chemical Society, 2023. **146**(1): p. 101-105.
28. Kamat, P.V., *Manipulation of charge transfer across semiconductor interface. A criterion that cannot be ignored in photocatalyst design.* The journal of physical chemistry letters, 2012. **3**(5): p. 663-672.
29. Zhang, B., et al., *Simultaneous Ni nanoparticles decoration and Ni doping of CdS nanorods for synergistically promoting photocatalytic H2 evolution.* Applied Surface Science, 2020. **508**: p. 144869.
30. Krishnapriya, R., S. Praneetha, and A.V. Murugan, *Microwave-solvothermal synthesis of various TiO 2 nano-morphologies with enhanced efficiency by incorporating Ni nanoparticles in an electrolyte for dye-sensitized solar cells.* Inorganic Chemistry Frontiers, 2017. **4**(10): p. 1665-1678.
31. Jaji, N.-D., et al., *Advanced nickel nanoparticles technology: From synthesis to applications.* Nanotechnology reviews, 2020. **9**(1): p. 1456-1480.
32. Li, Z., C. Han, and J. Shen, *Reduction of Ni 2+ by hydrazine in solution for the preparation of nickel nano-particles.* Journal of materials science, 2006. **41**: p. 3473-3480.
33. Cheng, R., et al., *Efficient photocatalytic CO2 reduction with MIL-100 (Fe)-CsPbBr3 composites.* Catalysts, 2020. **10**(11): p. 1352.
34. Parvinizadeh, F. and A. Daneshfar, *Fabrication of a magnetic metal–organic framework molecularly imprinted polymer for extraction of anti-malaria agent hydroxychloroquine.* New Journal of Chemistry, 2019. **43**(22): p. 8508-8516.

35. Jose, L.M., et al., *Adsorption and photocatalytic activity of biosynthesised ZnO nanoparticles using Aloe Vera leaf extract.* Nano Express, 2021. **2**(1): p. 010039.
36. Hajiali, M., M. Farhadian, and S. Tangestaninejad, *Novel ZnO nanorods/Bi2MoO6/MIL-101 (Fe) heterostructure immobilized on FTO with boosting photocatalytic activity for tetracycline degradation: Reaction mechanism and toxicity assessment.* Applied Surface Science, 2022. **602**: p. 154389.
37. Shakoor, M.N., et al., *Photodynamic effect of NiO in HepG2 cellular model.* Journal of Nanoelectronics and Optoelectronics, 2016. **11**(3): p. 339-342.
38. Hao, Q., et al., *Boosting Electrochemical Carbon Dioxide Reduction on Atomically Dispersed Nickel Catalyst.* Frontiers in Chemistry, 2022. **9**: p. 837580.
39. Vijaya Kumar, P., A. Jafar Ahamed, and M. Karthikeyan, *Synthesis and characterization of NiO nanoparticles by chemical as well as green routes and their comparisons with respect to cytotoxic effect and toxicity studies in microbial and MCF-7 cancer cell models.* SN Applied Sciences, 2019. **1**: p. 1-15.
40. Lv, H., et al., *Efficient degradation of high concentration azo-dye wastewater by heterogeneous Fenton process with iron-based metal-organic framework.* Journal of Molecular Catalysis A: Chemical, 2015. **400**: p. 81-89.
41. Chen, X., et al., *Preparation of ZnO Photocatalyst for the Efficient and Rapid Photocatalytic Degradation of Azo Dyes.* Nanoscale Research Letters, 2017. **12**(1): p. 143.
42. Shahzadi, T., et al., *Sulfate and phosphate ions removal using novel nano-adsorbents: modeling and optimization, kinetics, isotherm and thermodynamic studies.* International Journal of Phytoremediation, 2022. **24**(14): p. 1518-1532.
43. Ke, X., et al., *Highly augmented antioxidant and anticancer effect of biocompatible MIL-100 (Fe)@ SiO 2-immobilized green tea Catechin.* Journal of Inorganic and Organometallic Polymers and Materials, 2020. **30**: p. 935-942.
44. Musić, S., et al., *Influence of synthesis procedure on the formation and properties of zinc oxide.* Journal of alloys and compounds, 2002. **347**(1-2): p. 324-332.
45. Al-Shabib, N.A., et al., *Biofabrication of Zinc Oxide Nanoparticle fromOchradenus baccatusLeaves: Broad-Spectrum Antibiofilm Activity, Protein Binding Studies, andIn VivoToxicity and Stress Studies.* Journal of Nanomaterials, 2018. **2018**: p. 1-14.
46. Khan, G., *Optical band gap engineering of ZnO nanophosphors via Cu incorporation for ultraviolet–violet LED.* The European Physical Journal Plus, 2020. **135**(8): p. 684.
47. Das, S. and T. Alford, *Structural and optical properties of Ag-doped copper oxide thin films on polyethylene napthalate substrate prepared by low temperature microwave annealing.* Journal of applied physics, 2013. **113**(24).
48. de Souza, M.L., D.P. Dos Santos, and P. Corio, *Localized surface plasmon resonance enhanced photocatalysis: an experimental and theoretical mechanistic investigation.* RSC advances, 2018. **8**(50): p. 28753-28762.
49. Lv, S., et al., *Review on LSPR assisted photocatalysis: effects of physical fields and opportunities in multifield decoupling.* Nanoscale Advances, 2022. **4**(12): p. 2608-2631.
50. Sing, K., *The use of nitrogen adsorption for the characterisation of porous materials.* Colloids and Surfaces A: Physicochemical and Engineering Aspects, 2001. **187**: p. 3-9.
51. Jabbari, V., et al., *Green synthesis of magnetic MOF@ GO and MOF@ CNT hybrid nanocomposites with high adsorption capacity towards organic pollutants.* Chemical Engineering Journal, 2016. **304**: p. 774-783.

52. Liu, L., et al., *MIL‐100 (Fe) Supported Pt− Co Nanoparticles as Active and Selective Heterogeneous Catalysts for Hydrogenation of 1, 3‐Butadiene.* ChemistryOpen, 2022. **11**(3): p. e202100288.
53. Turchi, C.S. and D.F. Ollis, *Mixed reactant photocatalysis: intermediates and mutual rate inhibition.* Journal of Catalysis, 1989. **119**(2): p. 483-496.
54. Ho, Y.-S. and G. McKay, *Pseudo-second order model for sorption processes.* Process biochemistry, 1999. **34**(5): p. 451-465.
55. Mittal, A., et al., *Studies on the adsorption kinetics and isotherms for the removal and recovery of Methyl Orange from wastewaters using waste materials.* Journal of hazardous materials, 2007. **148**(1-2): p. 229-240.
56. Riahi, K., S. Chaabane, and B.B. Thayer, *A kinetic modeling study of phosphate adsorption onto Phoenix dactylifera L. date palm fibers in batch mode.* Journal of Saudi Chemical Society, 2017. **21**: p. S143-S152.
57. Guo, X.-Z., et al., *Effect of synergistic interplay between surface charge, crystalline defects, and pore volume of MIL-100 (Fe) on adsorption of aqueous organic dyes.* Industrial & Engineering Chemistry Research, 2020. **59**(5): p. 2113-2122.
58. Fang, Y., et al., *MIL-100 (Fe) and its derivatives: from synthesis to application for wastewater decontamination.* Environmental Science and Pollution Research, 2020. **27**: p. 4703-4724.
59. Kosmulski, M., *The pH dependent surface charging and points of zero charge. IX. Update.* Advances in Colloid and Interface Science, 2021. **296**: p. 102519.
60. Rafiq, A., et al., *Photocatalytic degradation of dyes using semiconductor photocatalysts to clean industrial water pollution.* Journal of Industrial and Engineering Chemistry, 2021. **97**: p. 111-128.
61. Yudasari, N., et al., *Enhanced photocatalytic degradation of rhodamine 6G (R6G) using ZnO–Ag nanoparticles synthesized by pulsed laser ablation in liquid (PLAL).* Journal of Alloys and Compounds, 2021. **886**: p. 161291.
62. Cabello-Guzmán, G., et al., *A photochemical approach to the synthesis of ZnO/CuO films and their application to the photocatalytic degradation of rhodamines (Rh-B and Rh-6G) under UV–Vis light irradiation.* Inorganic Chemistry Communications, 2023. **152**: p. 110695.
63. Asiri, A.M., et al., *Photodegradation of Rhodamine 6G and phenol red by nanosized TiO2 under solar irradiation.* Journal of Saudi Chemical Society, 2011. **15**(2): p. 121-128.
64. Ghorai, T.K. and N. Biswas, *Photodegradation of rhodamine 6G in aqueous solution via SrCrO4 and TiO2 nano-sphere mixed oxides.* Journal of materials research and technology, 2013. **2**(1): p. 10-17.
65. Nahyoon, N.A., et al., *Synthesis of novel visible light driven MgO@ GO nanocomposite photocatalyst for degradation of Rhodamine 6G.* Optical Materials, 2023. **135**: p. 113260.
66. Aziz, N., C. Sheng, and H. Jie, *Water remediation capability of cubic-phase CdS nanoparticles as photocatalyst on photodegradation of aqueous Rhodamine 6G dye under UV irradiation.* Dig. J. Nanomater. Biostruct., 2023. **18**: p. 203-210.
67. Khan, J., et al., *Controlled synthesis of ammonium manganese tri-fluoride nanoparticles with enhanced electrochemical performance.* Materials Research Express, 2019. **6**(7): p. 075074.

68. Khan, J., et al., *Synthesis, characterization and electrochemical performance of cobalt fluoride nanoparticles by reverse micro-emulsion method.* Inorganic Chemistry Communications, 2018. **98**: p. 132-140.
69. Al-Gaashani, R., et al., *Investigation of the optical properties of Mg (OH) 2 and MgO nanostructures obtained by microwave-assisted methods.* Journal of Alloys and Compounds, 2012. **521**: p. 71-76.
70. Lim, J., et al., *Optical modification of atomic thickness graphene oxide*. Int Soc Opt Photon. doi, 2012. **10**(2.1201210): p. 004520.
71. Bhargava, R. and S. Khan, *Superior dielectric properties and bandgap modulation in hydrothermally grown Gr/MgO nanocomposite.* Physics Letters A, 2019. **383**(14): p. 1671-1676.
72. Radulović, S., et al., *Three-dimensional SEM, TEM, and STEM for analysis of large-scale biological systems.* Histochemistry and Cell Biology, 2022. **158**(3): p. 203-211.
73. Dariani, R., et al., *Photocatalytic reaction and degradation of methylene blue on TiO2 nano-sized particles.* Optik, 2016. **127**(18): p. 7143-7154.

Supporting information

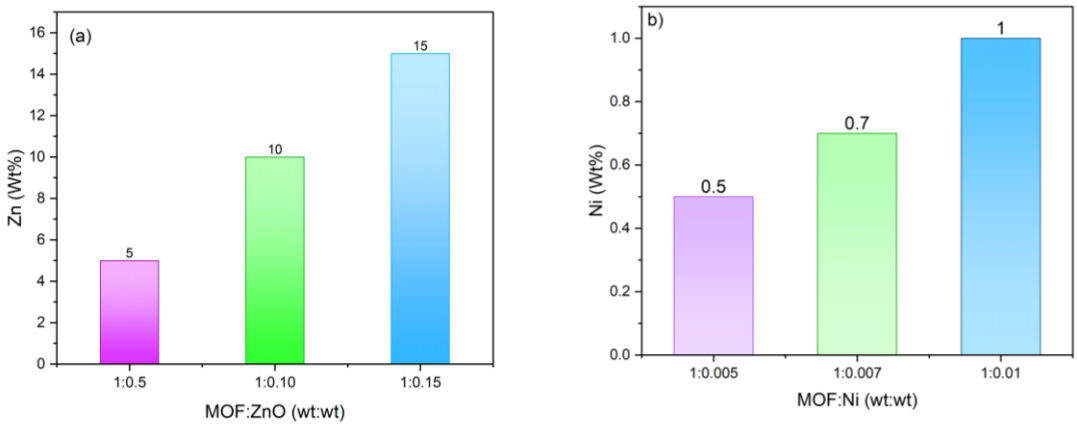

Figure S1. ICP-MS results of loading a) ZnO and b) Ni NPs in the synthesized composites.

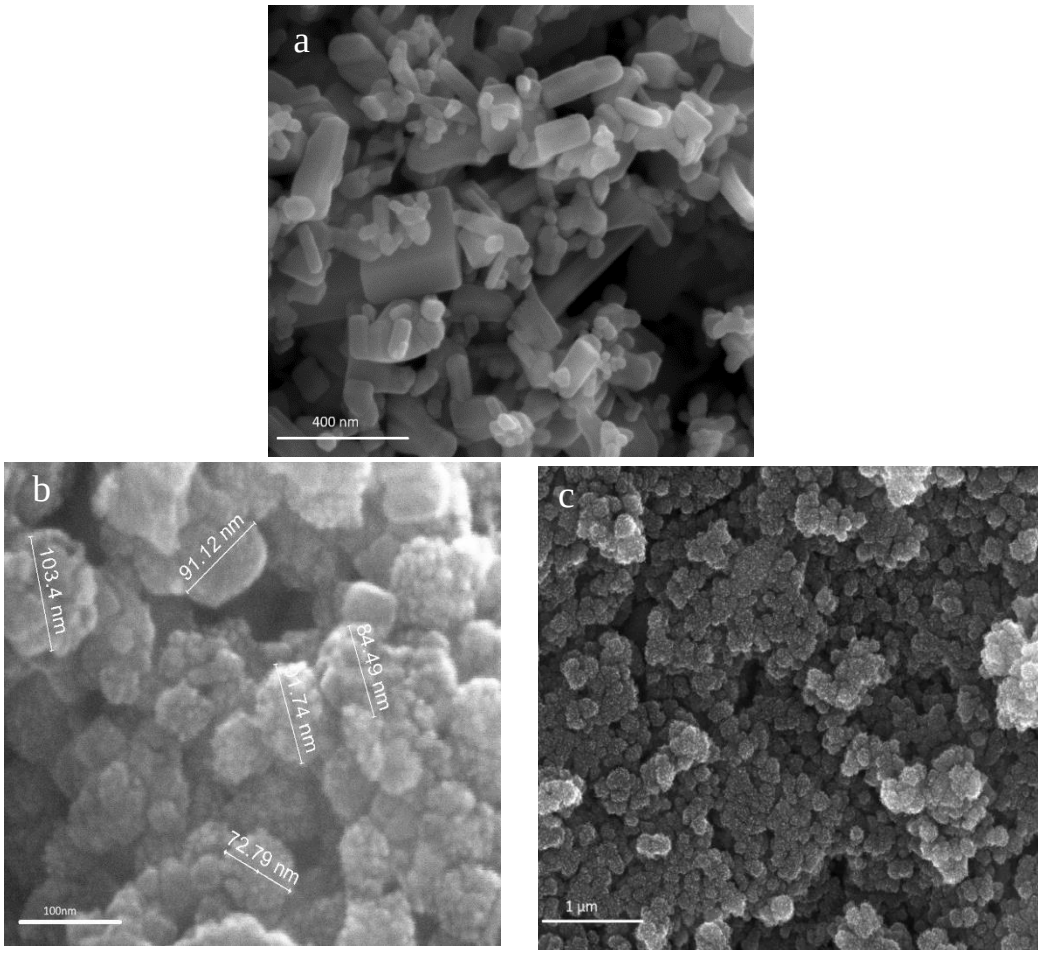

Figure S2. SEM image of a) commercially purchased ZnO NPs b) MIL-100(Fe) and c) Ni@MIL-100(Fe)

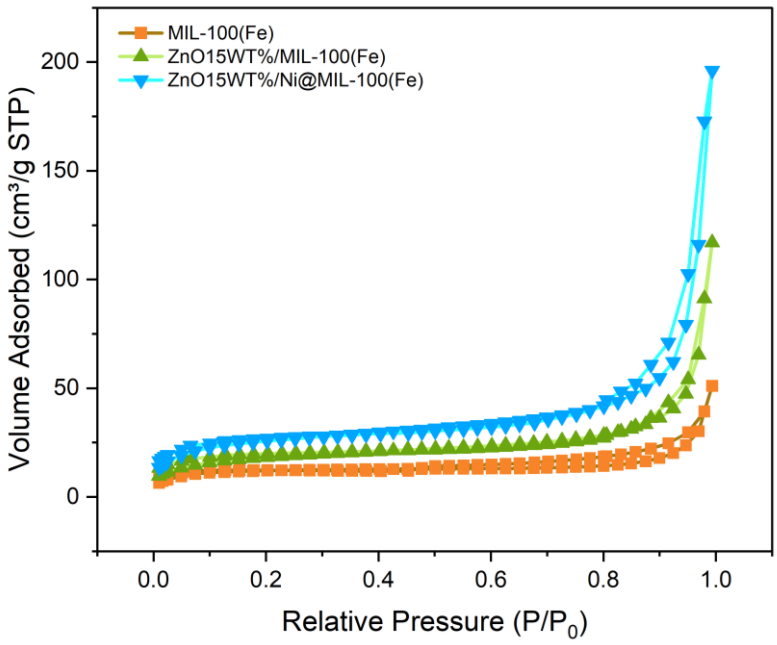

Figure S3.Nitrogen adsorption-desorption isotherms of MIL-100(Fe), ZnO15WT%/MIL-100(Fe), and ZnO15WT%/Ni@MIL-100(Fe)

Table S1.Textural properties of the ZnO/MIL-100(Fe) and ZnO/Ni@MIL-100(Fe) Samples with Different ZnO and Ni Nanoparticle Loadings

Catalyst	S_{BET} ($m^2\ g^{-1}$)	V_p ($cm^3\ g^{-1}$)	D(nm)
$ZnO_{0.05}$/MIL-100(Fe)	23.2179	0.000474	14.7437
$ZnO_{0.1}$/MIL-100(Fe)	61.2662	0.010148	8.995
$ZnO_{0.15}$/ $Ni_{0.007}$@MIL-100(Fe)	89.9581	0.01144	5.8543
$ZnO_{0.15}$/ $Ni_{0.01}$@MIL-100(Fe)	154.6315	0.047469	2.3214

Table S2.Adsorption kinetics of the materials from pseudo-second-order kinetics

Catalyst	K_2	R^2
ZnO NPs	0.254	0.99
MIL-100(Fe)	0.180	0.99
Ni@MIL-100(Fe)	0.071	0.99
ZnO/MIL-100(Fe)	0.194	0.99
ZnO /Ni@MIL-100(Fe)	0.038	0.99

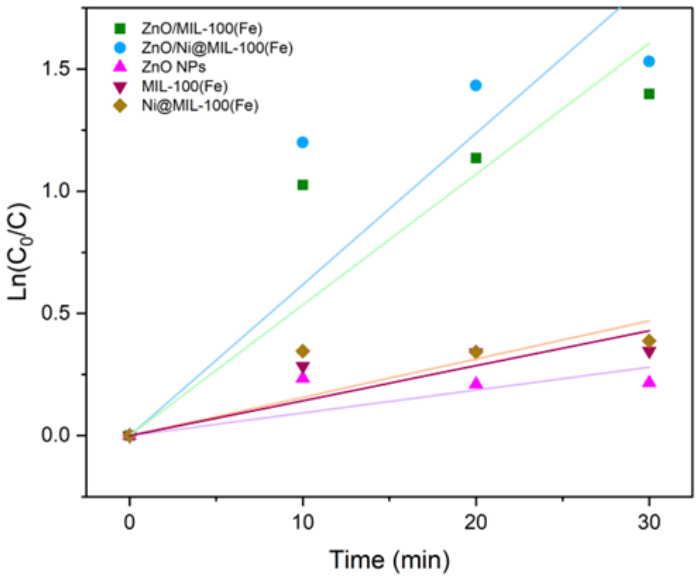

Figure S4.First order linear transforms of R6G adsorption by ZnO NPs, MIL-100(Fe), Ni@MIL-100(Fe), ZnO/MIL-100(Fe) and ZnO/Ni@MIL-100(Fe).

Table S 3. Adsorption kinetic parameters obtained from pseudo-first-order kinetics model.

Catalyst	**k**	**R^2**
ZnO NPs	0.0093	0.8319
MIL-100(Fe)	0.0143	0.9061
Ni@MIL-100(Fe)	0.0156	0.8881
ZnO/MIL-100(Fe)	0.0535	0.9329
ZnO /Ni@MIL-100(Fe)	0.0618	0.9175

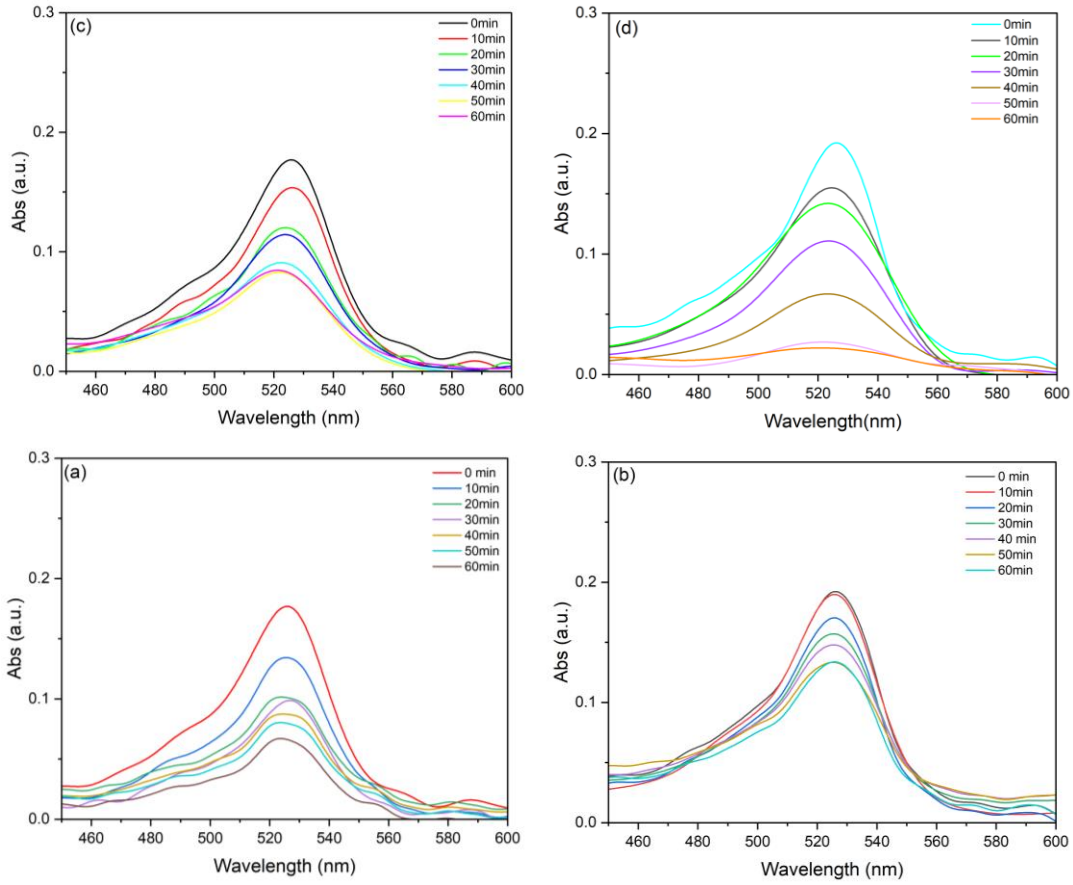

Figure S5. UV–vis absorption spectra of Rh6G solution during the photodegradation over a) ZnO /Ni@MIL-100(Fe) b) and ZnO/MIL-100(Fe) under visible light irradiation and c) ZnO /Ni@MIL-100(Fe) d) and ZnO/MIL-100(Fe) under UV irradiation.

Table S4. Photocatalytic degradation efficiencies of Rhodamine 6G using various catalysts under different light sources.

Catalyst	Light Source	Efficiency (%)	Time	Reference
ZnO/CuO films	UV–Vis light (Osram ultra-vitalux 300 W, 280–1000 nm)	68.3	300 min	[62]
QD/Eu-MOF	UV light (125 W high-pressure mercury vapor lamp, 365 nm)	>98	50 min.	[22]
n-TiO2	solar irradiation	98.99	140 min	[63]
ZnO–Ag nanoparticles	four x 8 W UV lamps	90	120 min	[61]
SrCrO4	400-W Hg lamp with wavelength of 364 nm.	97.5	3 h	[64]
MgO/GO	Tungsten light (50 W),	98		[65]
CdS nanoparticles	UV irradiation	24.68	180 min	[66]
GO/TiO	Halogen(250W) Tungsten (125 W)	82.9	240min	[67]
PANI/PbS	Tungsten (125 W)	87	50 min	[68]
ZnO-rGO	White light (100 W)	78	160 min	[69]
Porphyrin based SURMOF/GO	Halogen(150W)	90	10 min	[70]
5wt%CuO NPs/ZIF-8	UV–visible	96	105 min	[71]
CaMn3O6	Visible	83.1	240 min	[72]
ZnO/Zn film Rh6G	UV	34	30 min	[73]
ZnO /Ni@MIL-100(Fe)	20 W TUNGSTE N HALOGEN lamp emitting light with a wavelength range of 360 nm to 2.4 μm)	>98	60 min	This work
ZnO/MIL-100(Fe)	20 W TUNGSTE N HALOGEN lamp emitting light with a wavelength range of 360 nm to 2.4 μm)	>88	60 min	This work
ZnO/MIL-100(Fe)	Pencil UVC, wavelength = 254nm	>99	60 min	This work
ZnO /Ni@MIL-100(Fe)	Pencil UVC, wavelength = 254nm	>96	60 min	This work

.